University of Reading

Intraseasonal soil moisture-atmosphere feedbacks on the Tibetan Plateau circulation

Article

Accepted Version

Talib, J., Taylor, C.M., Duan, A. and Turner, A. ORCID: https://orcid.org/0000-0002-0642-6876 (2021) Intraseasonal soil moisture-atmosphere feedbacks on the Tibetan Plateau circulation. Journal of Climate, 34 (5). pp. 1789-1807. ISSN 1520-0442 doi: 10.1175/JCLI-D-20-0377.1 Available at https://centaur.reading.ac.uk/90790/

It is advisable to refer to the publisher's version if you intend to cite from the work. See Guidance on citing.

To link to this article DOI: http://dx.doi.org/10.1175/JCLI-D-20-0377.1

Publisher: American Meteorological Society

All outputs in CentAUR are protected by Intellectual Property Rights law, including copyright law. Copyright and IPR is retained by the creators or other copyright holders. Terms and conditions for use of this material are defined in the End User Agreement.

www.reading.ac.uk/centaur

University of Reading

CentAUR

Central Archive at the University of Reading

Reading's research outputs online

Intraseasonal soil moisture-atmosphere feedbacks on the Tibetan Plateau circulation

Joshua Talib *

UK Centre for Ecology and Hydrology, Wallingford, UK

Christopher M. Taylor

UK Centre for Ecology and Hydrology and National Centre for Earth Observation, Wallingford, UK

Anmin Duan

State Key Laboratory of Numerical Modelling for Atmospheric Sciences and Geophysical Fluid Dynamics, Institute of Atmospheric Physics, Chinese Academy of Science (CAS), Beijing 100029, China

Andrew G. Turner

Department of Meteorology, University of Reading, UK and National Centre for Atmospheric Science, University of Reading, UK

Corresponding author address: UK Centre for Ecology and Hydrology, Wallingford, UK

E-mail: jostal@ceh.ac.uk

ABSTRACT

Substantial intraseasonal precipitation variability is observed across the Tibetan Plateau (TP) during boreal summer associated with the subtropical jet location and the Silk Road pattern. Weather station data and satellite observations highlight a sensitivity of soil moisture and surface fluxes to this variability. During rain-free periods of two or more days, skin temperatures are shown to rise as the surface dries, signalling decreased evaporative fraction. Surface fluxes are further enhanced by relatively clear skies. In this study we use an atmospheric reanalysis to assess how this surface flux response across the TP influences local and remote conditions.

Increased surface sensible heat flux induced by decreased soil moisture during a regional dry event leads to a deepening of the planetary boundary-layer and the development of a heat low. Consistent with previous studies, heat low characteristics exhibit pronounced diurnal variability driven by anomalous daytime surface warming. For example, low-level horizontal winds are weakest during the afternoon and intensify overnight when boundary-layer turbulence is minimal. The heat low favours an upper-tropospheric anticyclone which induces an upper-level Rossby wave and leads to negative upper-level temperature anomalies across southern China. The Rossby wave intensifies the upper-level cyclonic circulation across central China, whilst upper-level negative temperature anomalies across south China extends the west Pacific subtropical high westward. These circulation anomalies influence temperature and precipitation anomalies across much of China. The association between land-atmosphere interactions across the TP, large-scale atmospheric circulation characteristics, and precipitation in east Asia highlights the importance of intraseasonal soil moisture dynamics on the TP.

1. Introduction

With an average height of 4500m and an area of approximately 2.5 million km^2, dynamic and thermodynamic processes over the Tibetan Plateau (TP, shown in Fig. 1a at approximately 28 to 40°N and 80 to 105°E) influence the large-scale atmospheric circulation across Eurasia. The TP surface provides a mid-tropospheric heat source in the mid-latitudes that opposes the textbook view of the zonal-mean Hadley circulation, intensifies the Indian and East Asian monsoons (Kutzbach et al. 1993; Molnar et al. 1993; Zhisheng et al. 2001; Duan and Wu 2005; Jiang et al. 2008), and varies the East Asian subtropical front location (Jiang et al. 2008; Wang et al. 2008; Liu et al. 2012; Wang et al. 2014). Substantial efforts have taken place to understand the sensitivity of interannual precipitation variability to TP land surface warming (Li and Yanai 1996; Duan and Wu 2005; Liu et al. 2012; Wang et al. 2014). However, there has been less attention paid to the impact of intraseasonal TP surface warming on atmospheric conditions.

Surface sensible heat flux (SHF) is controlled by incoming radiation, temperature, humidity, low-level wind, and land surface characteristics. Certain land surface properties such as vegetation cover, leaf area, and aerodynamic roughness change relatively slowly over the season. Meanwhile soil moisture, particularly near the surface, fluctuates strongly in response to rainfall, and decreases more gradually during dry spells. When vegetation is sparse, surface fluxes are sensitive to soil moisture due to substantial variations in evaporation. A recent observational study at a weather station located in a semi-arid region that extends across the central TP highlights that sub-seasonal variations in evaporation are predominately due to changes in soil evaporation rather than plant transpiration (Cui et al. 2020). Favouring of surface SHF over surface latent heat flux (LHF) during periods of soil moisture deficiency increases near-surface air temperatures (Koster et al. 2009; Miralles et al. 2012; Berg et al. 2014; Schwingshackl et al. 2017) and impacts

boundary-layer and large-scale circulation characteristics (Notaro and Zarrin 2011; Xue et al. 2012; Wan et al. 2017). Variations in surface fluxes also influence the intensity of drought and heatwave events (Zampieri et al. 2009; Weisheimer et al. 2011; Loikith and Broccoli 2012; Quesada et al. 2012; Chiriaco et al. 2014; Schumacher et al. 2019). In this study the sensitivity of surface fluxes and the atmospheric circulation to intraseasonal precipitation and soil moisture variability across the TP is investigated. In particular the influence of soil moisture deficiency across the TP on the development of heat lows and remote atmospheric conditions is explored.

Numerous observational and modelling studies demonstrate a sensitivity of local and remote atmospheric conditions to land surface characteristics on intraseasonal to interannual timescales. For example, interannual boreal summer rainfall variability across southern North America (Carleton et al. 1990) is associated with land surface characteristics across mountainous regions in western North America (Gutzler 2000; Lo and Clark 2002; Hu and Feng 2004; Notaro and Zarrin 2011; Xue et al. 2012, 2016, 2018; Diallo et al. 2019). Anomalously deep snowpack across high terrain regions in western North America increases surface albedo and provides a more persistent soil moisture source associated with decreased lower-tropospheric temperatures, a reduced land-ocean thermal gradient, a delayed poleward migration of the North American monsoon, and negative rainfall anomalies across southwest North America (Gutzler 2000; Lo and Clark 2002; Notaro and Zarrin 2011). There is also a significant relationship between late spring land surface temperature anomalies across western North America and boreal summer precipitation over the Southern Great Plains (Xue et al. 2012, 2016, 2018; Diallo et al. 2019). A positive land surface temperature anomaly across western North America increases surface SHF and induces a positive mid-tropospheric geopotential anomaly, the development of a planetary wave train, a cyclonic anomaly over the Southern Great Plains and the favouring of positive boreal summer rainfall anomalies (Xue et al. 2016, 2018). Similar to mountainous regions in western

North America, the TP is also a high elevated region at a similar latitude to the sub-tropical jet. It is hypothesised that mechanisms responsible for atmospheric changes that occur across the TP and south-east Asia, associated with anomalous land surface characteristics, are similar to those observed in North America.

Heat lows are common across sub-tropical arid and semi-arid regions during months of high insolation. To understand heat lows across the TP, previous studies analysing heat lows in other sub-tropical regions can be drawn upon. Heat lows have been observed and analysed across West Africa (Parker et al. 2005; Sultan et al. 2007; Lothon et al. 2008), Angola (Howard and Washington 2018), the Iberian Peninsula (Hoinka and Castro 2003), and Pakistan/north-west India (Bollasina and Nigam 2011) amongst other locations. Idealised modelling studies have focused on understanding heat low dynamics across western Australia (Rácz and Smith 1999; Spengler et al. 2005) and regions of high elevation (Smith and Spengler 2011). Heat lows are formed when strong solar surface heating leads to ascent and increased low-level relative vorticity. Even though low-level atmospheric temperatures maximise during the afternoon alongside a surface pressure minima at the centre of heat lows, boundary-layer turbulence inhibits and delays a low-level wind response. As a result, low-level convergence and relative vorticity do not maximise until nighttime, once insolation is removed and boundary-layer turbulence is much weaker (Rácz and Smith 1999; Parker et al. 2005; Smith and Spengler 2011; Howard and Washington 2018). Above the heat low, an anticyclone develops associated with upper-level divergence. Upper-level anticyclone characteristics have smaller diurnal variations compared to the low-level cyclone due to a reduced influence of diurnally-varying boundary-layer turbulence at altitude (Rácz and Smith 1999; Howard and Washington 2018). Idealised modelling experiments have also been performed to investigate the sensitivity of heat lows to orography (Smith and Spengler 2011). When applying identical surface heating to elevated and low regions, greater decreases in low-level air density are

simulated over elevated regions associated with a shallower atmosphere. The horizontal gradient in atmospheric density enhances low-level convergence and promotes an intensified heat low across elevated slopes. There are currently a small number of studies analysing the impact of intraseasonal soil moisture variations on the development of heat lows across semi-arid regions (Taylor 2008; Lavender et al. 2010). In this study we highlight the influence of intraseasonal soil moisture variability on heat low development across the TP using observations and reanalysis.

Modelling experiments highlight a sensitivity of local atmospheric conditions to TP surface warming (Wang et al. 2008; Liu et al. 2012; Wan et al. 2017; Ge et al. 2019). Increased TP surface warming promotes a heat low circulation associated with an anomalous low-level cyclone and an anomalous upper-level anticyclone (Wang et al. 2008; Wan et al. 2017; Ge et al. 2019). Alongside a local atmospheric response to TP surface warming, remote atmospheric conditions are also impacted (Wang et al. 2008; Wan et al. 2017). Wan et al. (2017) investigated the impact of initial soil moisture conditions across the TP in the Weather Research and Forecasting (WRF) model on local and remote atmospheric conditions. Their study was motivated by ten extreme precipitation events in southeast China, not associated with tropical cyclones, being preceded by anomalous positive TP near-surface air temperatures of approximately 1 to 2°C five days before. Three experiments were performed comparing a realistic soil moisture initialisation with idealised wet and dry soil conditions representing the two extremes in surface hydrology. Dry soil conditions increase surface SHF, boundary-layer height, and near-surface air temperatures across the TP. Low-level atmospheric heating induces an anomalous low-level cyclone, associated with positive temperature anomalies, and an upper-level anticyclone, associated with negative temperature anomalies. The upper-level anticyclone interacts with the subtropical Eurasian jet and induces an eastward-propagating Rossby wave, similar to behaviour observed across elevated regions in North America (Xue et al. 2016, 2018). The subtropical Eurasian jet also promotes the eastward

propagation of upper-level negative temperature anomalies. The combination of an upper-level Rossby wave and upper-level negative temperature anomalies induces a low-level cyclone across southeast China and extends the subtropical west Pacific high westward over central China. These two changes restrict the northward propagation of cyclonic circulations that develop in the South China sea and increase precipitation across southeast China. Changes in precipitation across China several days after surface drying on the TP highlight that land-atmosphere feedbacks across the TP can influence precipitation in East Asia.

In this study we will show the influence of intraseasonal soil moisture fluctuations across the TP, predominately controlled by precipitation variations, on the local surface energy balance. Following this, we will build on simulations analysed in Wan et al. (2017) to investigate the impact of surface flux variations, induced by soil moisture fluctuations, on heat low development across the TP and atmospheric conditions across East Asia. Through analysing this series of processes, we are investigating the full feedback cycle between the atmosphere drying and warming the surface and the land surface heating the atmosphere and modulating the circulation. Section 2 provides an overview of weather station datasets, satellite products and ERA5 (European Centre for Medium-Range Weather Forecasts Reanalysis version 5; Copernicus Climate Change Service (C3S) 2017; Hersbach et al. 2020) reanalysis that are utilised in this study. The results are presented in section 3 and are split into three components. Section 3a discusses the sensitivity of surface fluxes to intraseasonal precipitation and soil moisture variability across the TP, whilst sections 3b and 3c discuss the sensitivity of local and remote, respectively, atmospheric conditions to TP surface warming. Finally sections 4 and 5 provide a discussion and conclusions.

2. Methodology

In this study we use a combination of in situ weather station measurements, satellite products, and an atmospheric reanalysis to investigate the impact of soil moisture-atmosphere feedbacks across the TP. A network of 49 stations (cyan squares in Fig. 1a) above 3000m from the China Meteorological Administration (CMA) taking six-hourly (00, 06, 12 and 18 UTC) measurements between 2000 and 2015 of surface temperature (T_s), near-surface air temperature (T_a), and 10m wind speed (v_{10}), alongside daily precipitation accumulations at 12 UTC, are used to analyse surface conditions across the TP. CMA in situ measurements were only available between 2000 and 2015. To increase the number of years of precipitation data across the TP, we use daily precipitation accumulations extracted from APHRODITE (Asian Precipitation - Highly-Resolved Observational Data Integration Towards Evaluation; Yatagai et al. 2012) at 0.25° resolution from 1979 to 2015. APHRODITE is a gridded, continental-scale precipitation and near-surface air temperature product that utilises a dense network of weather stations (Yasutomi et al. 2011; Yatagai et al. 2012). Substantial interpolation is required across the TP due to the small number of weather stations. Values at each 0.25° grid point in APHRODITE are calculated by combining surrounding weather station measurements with locations approximated onto a 0.05° grid (Yatagai et al. 2012). In the case where zero rainfall measurements are taken across the 0.05° grid associated with a 0.25° grid point, interpolation is required from surrounding 0.25° grid values. To minimise the influence of interpolation, 0.25° grid points in APHRODITE are only analysed if they contain measurements for at a least one of the 0.05° grid points for a minimum of 95% of boreal summer days between 1979 and 2015. Even though APHRODITE comprises measurements from 26 different countries resulting in different times of day at which readings are taken (Yatagai et al. 2012), no spatial variations in the timing of measurements is recorded. As all measurements in

China are provided by CMA (Yatagai et al. 2012), the same organisation who provided the weather station data, we assume APHRODITE daily precipitation accumulations are computed at 12 UTC. We also use near-surface daily-mean air temperatures from APHRODITE to explore surface conditions during dry spells across the TP.

Several satellite products are used to understand the land surface response to intraseasonal precipitation variability across the TP. Precipitation data retrieved between 2000 and 2015 by the Tropical Rainfall Measuring Mission 3B42 version 7 (TRMM 3B42V7; Huffman et al. 2007) is utilised in this study. TRMM 3B42V7 precipitation data is computed by a combination of passive microwave data from low Earth-orbiting satellites, infrared data collected by the international constellation of geosynchronous earth orbit satellites, and monthly rain gauge data from the Global Precipitation Climatology Project (GPCP; Adler et al. 2003) and National Oceanic and Atmospheric Administration (NOAA) Climate Prediction Center (Huffman et al. 2007). Hourly-mean surface radiative fluxes are extracted from Clouds and the Earth's Radiant Energy System (CERES; Loeb et al. 2003) to understand changes in the surface energy balance across the TP. CERES surface fluxes are derived through combining (Kato et al. 2018): observed filtered top-of-the-atmosphere (TOA) irradiance in the shortwave and longwave (Loeb et al. 2003); cloud properties retrieved by Moderate Resolution Imaging Spectroradiometer (MODIS) and geostationary satellites (Minnis et al. 2011); and temperature, specific humidity, and ozone profiles from the Goddard Earth Observing System version 5.4.1 reanalysis (Rienecker et al. 2008). Finally, soil moisture anomalies across the TP are computed using satellite retrievals from the European Space Agency Climate Change Initiative (ESA CCI) combined soil moisture product v04.4 (Dorigo et al. 2017; Gruber et al. 2017, 2019). ESA CCI combined soil moisture product v04.4 combines four active and seven passive microwave-based instruments alongside a global land data assimilation system (GLDAS; Rodell et al. 2004) to obtain a consistent climatology throughout the entire time

series (Gruber et al. 2019).

CMA weather station data is used to approximate outgoing longwave radiation (LW_{up}) and surface SHF:

$$LW_{up} = \varepsilon \sigma T_s^4 \tag{1}$$

$$SHF = \rho C_p C_{DH} v_{10} (T_s - T_a) \tag{2}$$

where ε is the surface emissivity (assumed here to be fixed at 0.95); σ is the Stefan-Boltzmann constant (5.67×10^{-8} W m^{-2} K^{-4}), C_p is the specific heat capacity of dry air at constant pressure and equals 1005 J kg^{-1} K^{-1}; ρ is density (kg m^{-3}) and decreases exponentially with height; C_{DH} is the drag coefficient for heat and assumed at 4.0×10^{-3} for all stations (following Duan and Wu 2008); $\mathbf{v}_{10}$ is the mean wind measured at 10m above the ground (m s^{-1}); T_s and T_a are the skin and near-surface air temperatures (K) respectively. Combining CERES-derived surface fluxes with computed $\mathrm{LW_{up}}$ (Eqn. 1) and surface SHF (Eqn. 2) from CMA weather station data is used to partition the surface energy balance (SEB). The following equation is formulated after partitioning the SEB into land surface forcings and SEB components that depend on land surface characteristics:

$$SW_{net} + LW_{down} = LW_{up} + SHF + LHF + G \tag{3}$$

where $\mathrm{SW_{net}}$ denotes the surface net-downward shortwave radiation (W m^{-2}); $\mathrm{LW_{down}}$ denotes the surface downward longwave radiation (W m^{-2}); LHF denotes the latent heat flux (W m^{-2}); and G denotes the ground heat flux (W m^{-2}). If we assume that sub-seasonal changes in surface albedo are minimal, components on the right-hand side of (Eqn. 3) do depend on sub-seasonal changes

in surface characteristics whilst components on the left-hand side do not. Upon subtracting SHF and LW_{up} from CERES-derived surface radiation, the remainder is assumed to be a combination of LHF and G. In this study we only consider instantaneous surface fluxes at 18 UTC. We approximate instantaneous CERES-derived radiative fluxes by averaging hourly-mean retrievals at 1730 and 1830 UTC.

We use ERA5 reanalysis (Copernicus Climate Change Service (C3S) 2017; Hersbach et al. 2020) to investigate the influence of soil moisture-atmosphere interactions across the TP on local and remote atmospheric conditions. ERA5 data is analysed at a three-hourly 1° resolution on twenty pressure levels (50 to 1000hPa in increments of 50hPa). ERA5, computed using 4D-Var data assimilation and cycle 41r2 of the Integrated Forecasting System (IFS), provides a detailed record of the global atmosphere, land and ocean waves (Hersbach et al. 2018, 2020). At the time of access, ERA5 data was only available from 1979. Finally, due to the large longitudinal range with which Beijing Time (BT) is used across China, it is inappropriate to use BT as a reference for local solar conditions across the TP. In light of this we refer to the local solar time (LST) which is six hours ahead of UTC as the eastern TP is approximately situated at 90° longitude (Fig. 1a).

3. Results

a. Surface response to intraseasonal precipitation variability

1) INTRASEASONAL PRECIPITATION VARIABILITY

We first quantify boreal summer intraseasonal precipitation variability across the TP and east Asia (Fig. 1). To compute the annual-mean power associated with intraseasonal Boreal summer rainfall variability, the daily precipitation anomaly is standardised using the non-zero mean precipitation rate. Intraseasonal rainfall variability, shown in Figure 1a, is the total power

associated with modes between 7 and 30 days when performing a discrete Fourier transform on the standardised daily precipitation anomaly. In agreement with previous studies (Wang and Duan 2015), both standardised satellite and weather station data illustrate substantial intraseasonal precipitation variability across the TP (Fig. 1a, b). In comparison with intraseasonal precipitation variability across the rest of East Asia, the TP stands out along with the Indian monsoon core zone (approximately 16 to 22°N and 75 to 85°E; Mandke et al. 2007), associated with active and break spells of the Indian summer monsoon (Rajeevan et al. 2010; Singh et al. 2014), and the coast of Myanmar (approximately 20°N and 95°E), associated with orographically-driven precipitation (Shige et al. 2017). Greater daily precipitation accumulations over the ocean compared to land lead to a substantial land-sea contrast in intraseasonal precipitation variability. Note that the stronger power at intraseasonal timescales in CMA compared to APHRODITE (Fig. 1b) is due to APHRODITE being a gridded dataset whilst CMA is a set of localised weather stations (section 2).

We now exploit the availability of a network of long-term in situ surface temperature measurements from CMA and satellite soil moisture observations to examine the land surface response to intraseasonal precipitation variability across the TP. An initial look at a typical summer season (JJA 2013) illustrates that intraseasonal soil moisture fluctuations across the TP are strongly controlled by precipitation variations. As well as this, substantial changes in the five-day running-mean 12 LST surface temperature anomalies are broadly out of phase with rainfall (Fig. 1c). During periods of minimal rainfall, i.e. mid-June 2013, surface soil moisture decreases and skin temperature anomalies of approximately +10°C are observed at 12 LST. During wet periods, i.e. the majority of July 2013, surface soil moisture increases and negative skin temperatures anomalies of approximately -5°C are observed at 12 LST. Substantially smaller skin temperature anomalies are observed at other times of the day illustrating a diurnally-varying sensitivity of the

land surface to precipitation variability associated with the diurnal cycle of insolation. This time series suggests a strong sensitivity of daytime surface heating across the TP to dry events and qualitatively, similar features are found in every boreal summer of the CMA dataset (not shown).

2) Station-scale land surface response to dry events

To better understand the surface response to precipitation variability across the TP, a dry event composite is computed at each CMA weather station. Daily precipitation accumulations are used to identify "dry events". Similar to Gallego-Elvira et al. (2016), a dry event is defined when the initial precipitation rate is above 5 mm day^{-1} and succeeded by a least two days with less than 1 mm day^{-1}. In Gallego-Elvira et al. (2016), a maximum threshold of 0.5 mm day^{-1} is used to define a dry day. However, when compositing CMA weather station data this threshold gave a small number of dry events. In CMA approximately 3800 two-day dry events are observed between 2000 and 2015 with the number of dry events decreasing exponentially with dry event length (Fig. 2). We also composite the nearest ESA CCI soil moisture observation to each weather station during a dry event. Note that there are approximately 62% fewer observations of soil moisture than temperature in this composite due to limited availability in the ESA CCI dataset.

Compositing dry events across all weather stations illustrates a strong sensitivity of soil moisture and daytime skin temperatures to prolonged periods of minimal rainfall (Fig. 2a). As the surface dries, peak daytime skin temperatures increase by approximately 10°C in five days. The same diurnal variability is observed in near-surface air temperatures but to a smaller amplitude (only approximately 2°C in five days). As the surface SHF depends on the temperature difference between the ground and near-surface, Fig. 2a indicates that increasing daytime near-surface air temperatures during a prolonged period of minimal rainfall is surface-driven.

As expected from the smaller sensitivity of near-surface air temperatures to minimal precipitation compared to surface temperatures (Fig. 2a), anomalous daytime surface SHF increases with dry event length (Fig. 2b). Increasing surface temperatures are also associated with increasing LW_{up}. After five days of minimal rainfall, both SHF and LW_{up} have increased to approximately 50 W m^{-2}. The initial high precipitation accumulation at the start of a dry event is associated with cloud cover and daytime surface radiation anomalies of approximately -70 W m^{-2}. Surface radiation anomalies then increase to approximately 70 W m^{-2} by day 2 and remain relatively constant throughout the remainder of the dry event. As the inputted radiation anomaly remains relatively constant throughout the dry event composite, increased SHF and LW_{up} is associated with decreased LHF and G in order to maintain surface energy balance. This shows that the evaporative fraction, the fraction of turbulent energy fluxes used for evaporation, decreases as the dry spell length increases following high values on days 0 and 1. Even over short dry spells of two to three days, reduced soil moisture drives a shift in the partitioning of fluxes from latent to sensible heat. This is consistent with satellite-based analysis across semi-arid regions of the world (Gallego-Elvira et al. 2016). We also considered whether our dry spell flux composite was representative of all sites, or just those in climatologically drier regions. Compositing data from only the 10 wettest stations (boreal summer seasonal mean rainfall $\geq$ 2.27 mm day^{-1}), we still found a clear dry spell imprint on evaporative fraction (not shown), albeit of a slightly weaker amplitude than the full station composite, as expected.

3) Regional surface response to dry events

Individual weather stations highlight a sensitivity of local surface characteristics and SEB components to a prolonged period of minimal rainfall. In this subsection we investigate diurnal variations in land surface characteristics on a regional scale. We expect these to differ quantita-

tively due to the spatial scaling properties of rainfall.

Regional dry events are identified when the station-mean daily precipitation accumulation is below the boreal summer station-mean twentieth percentile for three consecutive days, having first removed periods with zero rainfall before calculating percentiles. Using this threshold for rainfall and dry event length reveals a suitable number of dry events across the TP required to obtain a substantial surface response. Thirty-seven three-day regional dry events are identified in the CMA dataset. During days of minimal precipitation, the composite-mean, station-mean daytime CMA near-surface air temperature anomalies increase to approximately 1.5°C (Fig. 3a). As seen on a localised scale (Fig. 2), skin temperatures are more sensitive to minimal rainfall than near-surface air temperatures with a peak anomaly just below 6°C (Fig. 3a). Focusing on SEB components observed at 12 LST highlights that the difference between anomalous skin and near-surface air temperatures is associated with an increased surface SHF of approximately 45 W m^{-2} and a decreased LHF and G total by approximately 50 W m^{-2} (Fig. 3b). During the dry event, anomalous daytime LHF decreases associated with surface drying; surface soil moisture observations from ESA CCI highlight a 10% reduction between the start and end of a three-day regional dry event (Fig. 3a). Surface soil moisture values from ERA5 and the Global Land Data Assimilation System (GLDAS) Noah Land Surface Model (Rodell et al. 2004) also reveal a similar sensitivity of soil moisture to regional dry spells (not shown). The diurnally-varying sensitivity of near-surface air and skin temperatures (Fig. 3a) is associated with a diurnally-varying sensitivity of SEB components (not shown). In the following section the sensitivity of the regional circulation to surface warming and increased surface SHF, associated with minimal precipitation and surface drying, is investigated.

Weather station data from CMA highlights the sensitivity of SEB components to minimal precipitation. However, due to data only being available from 2000 to 2015 (section 2), only 37

regional dry events are observed. To increase the number of regional dry events a composite using precipitation accumulations since 1979 from APHRODITE is produced. Seventy-two regional dry events are observed in APHRODITE, just under double the number of events observed in CMA. At a local scale the sensitivity of daily-mean near-surface air temperatures to minimal rainfall is similar in APHRODITE and CMA (Fig. 4). After five days of minimal rainfall, near-surface daily-mean air temperature anomalies are approximately 1.3°C in both datasets. After seven days of minimal rainfall, daily-mean air temperature anomalies continue to increase in CMA but plateau in APHRODITE, associated with a smaller number of localised dry events lasting longer than seven days in APHRODITE. Because the CMA and APHRODITE datasets share a similar sensitivity of daily-mean near-surface air temperature anomalies to minimal precipitation, we assume that the sensitivity of surface temperatures and SEB components is similar in regional dry events extracted from both datasets. As APHRODITE contains nearly double the number of three-day regional dry events compared to CMA (Fig. 3), the rest of this study focuses on regional dry events identified in APHRODITE.

b. Influence of TP surface warming on regional atmospheric conditions

In this section we consider how enhanced daytime surface heating on the TP during three-day regional dry events feeds back onto the atmosphere. However, we first examine the large-scale atmospheric conditions at the start of a regional dry event. At 200 hPa the beginning of a three-day dry event is associated with anomalous north-easterly winds across the western TP, an anomalous cyclone across east TP, and an anomalous anticyclone northwest of TP (Fig. 5a). The anomalous upper-level circulation pattern observed at the start of regional dry events is associated with the Silk Road pattern (SRP) teleconnection (Lu et al. 2002; Enomoto et al. 2003; Hsu and Lin 2007).

Forced by diabatic heating across the Eurasian continent (Hsu and Lin 2007), the SRP develops during boreal summer and is associated with a propagating Rossby wave along the subtropical Eurasian jet (Lu et al. 2002; Enomoto et al. 2003). The propagation of the SRP onto the TP is best observed in the vertically-averaged upper-tropospheric meridional wind (Fig. 6a). Significant meridional wind and geopotential anomalies are observed over Europe five to eight days before a dry event across the TP. At 500 hPa, approximately just above the east TP surface, anomalous northerly winds dominate at the beginning of a dry event associated with an anomalous anticyclone (Fig. 5b).

Temperature anomalies at 500 hPa across the TP during regional dry events increase by approximately 2.5°C (Fig. 6e). As surface warming peaks during daytime hours of regional dry events, we investigate sub-daily variations in atmospheric conditions to try to identify the surface influence on local atmospheric conditions. Sub-daily temperature variations at 500 hPa highlight that low-level warming predominately occurs during daytime hours (red line in Fig. 7a). The depth of positive temperature tendencies increases as the day progresses associated with a deepening boundary-layer (Figs. 7a and 8). Sub-daily tendencies in anomalous temperatures across the TP during regional dry events are similar to those in heat low studies that use idealised experiments (Rácz and Smith 1999; Smith and Spengler 2011) and observations (Hoinka and Castro 2003; Parker et al. 2005; Howard and Washington 2018). Sub-daily variations in geopotential height and surface pressure also resemble heat low characteristics with reductions in surface pressure and low-level geopotential height occurring after sunset (Fig. 7b, c). As described in Rácz and Smith (1999), substantial surface warming drives boundary-layer turbulence during the daytime which restricts a horizontal wind response to the developed pressure gradient. Once insolation is removed and the surface cools, a stable surface layer develops. This leads to minimal boundary-layer turbulence, allowing the horizontal flow to strengthen. Low-level zonal convergence and vertical ascent

develop in the evening across the eastern TP, with the latter extending to 200 hPa (Fig. 8h). The low-level (500 hPa) flow becomes more geostrophic during the evening and generates positive low-level relative vorticity (Fig. 9d).

Above the heat low an anticyclone develops at approximately 200 hPa associated with negative temperature tendencies (Fig. 8). Upper-level anticyclone characteristics vary diurnally, with positive geopotential tendencies reaching their maximum during the afternoon and evening (Fig. 8f, h) associated with sub-daily variations in mid-tropospheric warming between 250 and 400 hPa (Fig. 8e, g). Diurnal variations in upper-level anticyclonic characteristics are inconsistent with modelling work performed by Rácz and Smith (1999) due to diurnal variations in mid-tropospheric heating. Different mechanisms are responsible for mid-tropospheric heating during the afternoon and evening. In the afternoon mid-tropospheric warming is associated with a deepening of the boundary-layer, whilst mid-tropospheric warming during the evening, is associated with increased mid-tropospheric shear turbulence due to difference in wind direction between the sub-tropical westerly jet and easterly component of low-level convergence. Not only does anomalous turbulent mixing increase mid-tropospheric temperatures, but it also increases mid-tropospheric zonal wind (Fig. 8g) due to the downward transport of zonal momentum from the sub-tropical westerly jet (Fig. 10a). Warming between 250 and 400 hPa alongside cooling at 150 hPa increases geopotential height at 200 hPa. As expected, upper-level relative vorticity tendencies are also strongest during the afternoon and evening (not shown).

Regional-scale three-day dry spells across the TP, initially driven by upper-tropospheric geopotential anomalies, lead to surface warming, the formation of a heat low, and positive upper-level geopotential tendencies. In the following section we investigate the influence of positive geopotential upper-tropospheric tendencies, associated with the development of a heat low, on the remote circulation and weather conditions across east Asia.

c. Influence of TP surface warming on remote atmospheric conditions

Regional dry events across the TP favour the development of a heat low (section 3b). It is challenging to isolate the influence of anomalous atmospheric conditions across the TP on the remote atmospheric circulation using observations alone due to the influence of other factors, notably the large-scale circulation. However, Wan et al. (2017) performed modelling sensitivity experiments to investigate the influence of soil moisture across the TP on atmospheric conditions during an extreme rainfall event in southeast China. In this section we will compare remote atmospheric changes observed in our regional dry spell composite with the sensitivity of remote atmospheric conditions to TP soil moisture in Wan et al. (2017).

In Wan et al. (2017) extreme decreases in soil moisture across the TP increase surface SHF and lead to the development of a heat low. The heat low influences remote atmospheric conditions through two mechanisms: (1) the development of an upper-level planetary Rossby wave train; and (2) the eastward propagation of upper-level negative temperature anomalies. During our regional dry event composite negative upper-level geopotential tendencies are observed east of the TP alongside positive upper-level geopotential tendencies further east (Figs. 5c and 6b). The diurnal cycle of geopotential tendencies is approximately 20% greater east of the TP during the afternoon and evening (Fig. 8), the same time period where geopotential tendencies maximise due to the development of a heat low. Both of these factors are indicative of a Rossby wave forcing. In our composite the upper-level Rossby wave forcing associated with the heat low intensifies an upper-level cyclone east of TP across central China (Figs. 5c, 6b). The intensified upper-level cyclone also decreases geopotential height at 500 hPa, and by the end of the dry spell, significant negative geopotential anomalies are observed across central China at 200 and 500 hPa (Figs. 5 and 6). The upper-level Rossby wave forcing observed in our regional dry event composite

agrees well with Wan et al. (2017). However, Wan et al. (2017) show an intensified cyclone at 850 hPa over southeast China, meanwhile in our composite, geopotential height anomalies at 850 hPa are minimal at the end of dry events (Fig. 10d). It may also be argued that the SRP is solely responsible for geopotential tendencies observed. However, as upper-level anomalies in meridional wind and geopotential height dramatically decrease after day 3 (Fig. 6a, b), we infer that the SRP is not solely responsible for upper-level geopotential anomalies downstream of the TP during dry spells.

Alongside an immediate atmospheric response to heat lows across the TP due to Rossby wave forcing, the remote atmosphere is also influenced several days after regional dry events. Negative upper-level temperature anomalies associated with heat lows (Figs. 7a and 10c) propagate along the sub-tropical jet (Fig. 10a) reaching southern China three days after minimal precipitation across the TP (Figs. 6d and 10e). This advected cool upper-level air increases geopotential height beneath it and favours a westward extension of the western north Pacific sub-tropical high (Fig. 10f). In Wan et al. (2017) the advection of cool air generates positive geopotential height anomalies across central China, whilst in our dry event composite low-level geopotential height anomalies are much smaller and located over central and southern China (Fig. 10f). Even increasing the length of regional dry events to promote further surface drying across the TP and leading to surface soil moisture anomalies more similar to Wan et al. (2017), has a minimal effect on remote geopotential height anomalies (not shown). Advection of negative vorticity from an anticyclone northwest of TP (Fig. 5b) along the sub-tropical jet (Fig. 10a) leads to a broad region of positive geopotential anomalies across northern China (Fig. 5e, f).

To conclude our analysis we examine the association of dry events across the TP with weather conditions across East Asia. Dry events across the TP are associated with a dipole in daily-mean temperature changes (Fig. 11b, d, f, h). Several days after dry events across the TP, daily-mean

temperatures increase by 1.2°C across central and eastern China and decrease by 0.5°C in southeast China and the Indochinese peninsula. Figure 11h highlights that surface-atmosphere interactions across the TP during dry spells significantly increases near-surface temperatures across heavily populated and agriculturally intensive regions of East Asia. In Wan et al. (2017) reducing soil moisture across the TP increases total and extreme precipitation in southeast China. In our study a dipole in mean precipitation changes is observed several days after surface drying across the TP (Fig. 11a, c, e, g). Across central and eastern China mean precipitation significantly decreases whilst precipitation increases in southeast China and the Indochinese peninsula. During days 3 and 4 the dipole in mean precipitation changes is associated with an intensified cyclone across central China (Fig. 5c, d), whilst by day 6, the westward extension of the west Pacific sub-tropical high (Fig. 10f) restricts northward moisture propagation and increases precipitation across southern China. Wan et al. (2017) highlight an increased probability of extreme precipitation in southeast China when drying the TP surface. However in our composite, the increased likelihood of extreme precipitation in southeast China is insignificant (not shown). There are several reasons for the different responses in extreme precipitation. Firstly, Wan et al. (2017) only investigate the influence of soil moisture across the TP during a single extreme precipitation event where atmospheric conditions may not be typical for when the TP surface is dry. Secondly, soil conditions in our dry event composite are substantially less extreme than in sensitivity experiments by (Wan et al. 2017). As a result, surface sensible heat fluxes across the TP are much greater in Wan et al. (2017) compared to those in our dry event composite (Fig. 3b) by approximately 70 W m^2. Finally, the influence of tropical cyclones on extreme precipitation rates across East Asia have not been considered in this study. Hence, the influence of land-atmosphere interactions across the TP on extreme precipitation rates is challenging to detect due to the influence of tropical cyclones. Whilst the influence of dry events across the TP

on extreme precipitation rates requires further investigation, significant mean precipitation and temperature changes highlight the importance of land-atmosphere interactions.

4. Discussion

The warming rate of surface temperatures relative to near-surface air temperatures can be used to highlight the land surface response to dry spells (Gallego-Elvira et al. 2016). Combining in situ weather station measurements with satellite-derived datasets, we have highlighted the sensitivity of land surface characteristics across the TP to even short dry spells of two to three days. In situ measurement shown here reveal an average relative warming rate of approximately 0.38 K day^{-1} across the eastern TP for dry spells of approximately five days. During periods of minimal rainfall across the TP, surface LHF is limited, due to soil moisture availability, and surface SHF increases. In general, changes in evaporative fraction during dry spells are difficult to capture in climate models (Gallego-Elvira et al. 2019). Given the feedback on the atmosphere by the flux response to surface drying across the TP shown here and previous studies (Wan et al. 2017; Xue et al. 2018), analysis of model depictions of TP dry spells is warranted.

Through investigating the sensitivity of local atmospheric conditions to regional dry events across the TP we diagnose the formation of heat lows. In agreement with idealised modelling studies (Rácz and Smith 1999; Spengler et al. 2005; Smith and Spengler 2011) and observations of heat lows in other sub-tropical regions (Parker et al. 2005; Bollasina and Nigam 2011; Howard and Washington 2018), land-atmosphere interactions play a crucial role in the diurnal cycle of heat low characteristics. Whilst daytime surface heating reaches its maximum during the afternoon, boundary-layer turbulence inhibits a low-level horizontal wind response. Once insolation is removed and a stable surface layer develops, low-level horizontal convergence and relative

vorticity maximises. This is the first study to show how dry spells across the TP influence the diurnal cycle of heat lows. Even though idealised modelling studies conclude a minimal diurnal cycle of upper-level anticyclonic characteristics (Rácz and Smith 1999; Smith and Spengler 2011), we find that mid-tropospheric heating during the afternoon and evening, associated with increases in boundary-layer depth and mid-tropospheric turbulent mixing, result in sub-daily variations in anticyclonic characteristics.

The influence of land-atmosphere interactions on other circulation systems across the TP remains to be investigated. For example, Tibetan Plateau vortices (TPVs) are mesoscale circulations distinguished by substantial low-level relative vorticity and responsible for a substantial fraction of precipitation across the TP (Curio et al. 2019). In this study surface drying increases low-level relative vorticity thereby motivating future work to investigate the influence of land-atmosphere interactions in the development and intensity of TPVs. Recent studies have also shown that soil moisture gradients across the TP favour the initiation of convective systems (Barton et al. submitted).

Soil moisture-atmosphere interactions during dry events across the TP also influence atmospheric and weather conditions across east Asia. Previous observational and modelling studies have shown how large-scale surface temperature anomalies across the TP promote an atmospheric stationary wave that extends eastward from the original surface temperature anomaly (Wan et al. 2017; Xue et al. 2018). Our results are consistent with these findings. Future work should investigate whether these soil moisture-atmosphere feedbacks are observed in weather forecasting models to improve sub-seasonal forecasting capabilities across East Asia.

The sensitivity of remote atmospheric conditions to surface drying across the TP is substantially different in our dry event composite compared to sensitivity experiments performed by Wan et al. (2017). The difference in atmospheric response is most likely associated with the magnitude

of soil moisture forcing in these two studies. In Wan et al. (2017) soil moisture is reduced to the surface layer's wilting point, effectively fixing evapotranspiration to zero. In our dry event composite soil moisture fluctuations are much smaller and the change in latent heat flux is approximately 70 W m^{-2} smaller compared to latent heat flux changes when drying the TP in Wan et al. (2017). We therefore conclude that it is unrealistic to fix evapotranspiration to zero across the TP and the difference in soil moisture fluctuations leads to a much greater surface and atmospheric response in Wan et al. (2017). For example, the difference in surface SHF between a normal and dry TP surface is approximately three times greater in Wan et al. (2017) compared to anomalies observed in our dry event composite. Stronger surface SHF anomalies in Wan et al. (2017) promote an intensified localised heat low, colder upper-level temperature anomalies, and increased low-level geopotential height tendencies across east Asia. The westward extension of the western North Pacific sub-tropical high is further north in Wan et al. (2017) compared to changes observed in our dry event composite. This may be due to Wan et al. (2017) only performing sensitivity experiments for a single persistent heavy precipitation event in south-east China. The different atmospheric mean states and fluctuations in land surface characteristics between this study and sensitivity experiments analysed in Wan et al. (2017), vary the influence of land-atmosphere interactions across the TP on extreme precipitation events across east Asia. Surface conditions across East Asia may influence the atmospheric response to dry spells across the TP. For example, it may be the case that near-surface warming across north China several days after a TP dry spell would be larger during a local drought. However, the small number of dry spells in our sample precludes further subsetting. We would recommend a modelling approach to understand this dependence. Work in this study and by Wan et al. (2017) highlight the importance of land-atmosphere interactions across the TP in determining weather conditions across east Asia.

Improving the simulation of land-atmosphere interactions across the TP at all time scales may

lead to improvements in climate models over a much larger region. Warming across the TP provides a heat source in the mid-latitudes that intensifies the Indian monsoon (Kutzbach et al. 1993; Molnar et al. 1993; Zhisheng et al. 2001). Improving the sensitivity of surface temperatures to intraseasonal precipitation variability across the TP may intensify the Indian monsoon and partly improve the long-standing boreal summer dry bias across the Indian continent (Sperber et al. 2013; Bush et al. 2015). The influence of intraseasonal fluctuations in land surface characteristics across the TP should also be considered when predicting the atmospheric response to anthropogenic climate change across east Asia. Not only has anthropogenic climate change been associated with surface warming across the TP (Wang et al. 2008), but also substantial glacial loss (Yao et al. 2007, 2012), which may increase the area of semi-arid land and intraseasonal variability of surface fluxes. An increased influence of the TP land surface on local and remote atmospheric conditions may change weather conditions across east Asia.

5. Conclusions

Using a combination of weather station data and satellite observations we show that soil moisture and surface fluxes across the TP are sensitive to intraseasonal precipitation variability. Decreases in soil moisture during dry spells of even two to three days drive increases in surface temperatures and sensible heat fluxes. Atmospheric reanalysis shows how the anomalous surface warming feeds back onto the atmosphere and promotes the development of a heat low across the TP. Consistent with studies from other parts of the world, we illustrate strong diurnal variations in heat low characteristics. During daytime hours anomalous surface warming increases boundary-layer temperatures. However, boundary-layer turbulence restricts a low-level wind response until the surface cools and a stable layer develops. As a result, low-level horizontal convergence and

relative vorticity reach their maximum after sunset along with a reduction in surface pressure. Above the boundary-layer, heat lows promote an anticyclone associated with negative temperature anomalies. The local atmospheric response to surface warming due to precipitation variability across the TP highlights the importance of land-atmosphere interactions.

The development of heat lows across the TP also influences remote atmospheric conditions. The development of an upper-level anticyclone during dry spells promotes an upper-level stationary wave that intensifies a cyclonic circulation across central China. Negative temperature anomalies, associated with the upper-level anticyclone, propagate along the sub-tropical Eurasian jet towards south-east China, associated with a westward extension of the western North Pacific subtropical high. Both the intensification of a cyclonic circulation across central China and the westward extension of the western North Pacific subtropical high significantly impact weather conditions in east Asia. Understanding of land-atmosphere interactions across the TP is thus important for short-term weather forecasting across East Asia. Given the rapidly changing nature of the hydrological cycle on the TP in response to anthropogenic warming, it may also be relevant for climate projections across the region. Future work should therefore investigate the simulation of these soil moisture-atmosphere interactions in both weather and climate models.

Acknowledgments. This work and its contributors (JT, CT, AD, AT) were supported by the UK-China Research & Innovation Partnership Fund through the Met Office Climate Science for Service Partnership (CSSP) China as part of the Newton Fund.

The authors would like to express their gratitude to those at the Chinese Meteorological Administration for providing weather station data. APHRODITE precipitation and temperature data was accessed at http://www.chikyu.ac.jp/. TRMM 3B42V7 and CERES satellite products

were obtained from the NASA/Goddard Earth Sciences Data and Information Services Center (GES-DISC). ESA CCI soil moisture satellite data and ERA5 reanalysis data was accessed at https://www.esa-soilmoisture-cci.org/ and https://cds.climate.copernicus.eu/cdsapp/home respectively. We also thank three anonymous reviewers for their comments.

References

Adler, R. F., and Coauthors, 2003: The version-2 global precipitation climatology project (GPCP) monthly precipitation analysis (1979–present). *Journal of Hydrometeorology*, **4 (6)**, 1147–1167.

Barton, E., C. Taylor, C. Klein, P. Harris, and X. Meng, submitted: Observed soil moisture impact on strong convection over mountainous Tibetan Plateau. *Journal of Hydrometeorology*.

Berg, A., B. R. Lintner, K. L. Findell, S. Malyshev, P. C. Loikith, and P. Gentine, 2014: Impact of soil moisture–atmosphere interactions on surface temperature distribution. *Journal of Climate*, **27 (21)**, 7976–7993.

Bollasina, M., and S. Nigam, 2011: The summertime heat low over Pakistan/northwestern India: evolution and origin. *Climate Dynamics*, **37 (5-6)**, 957–970.

Bush, S. J., A. G. Turner, S. J. Woolnough, G. M. Martin, and N. P. Klingaman, 2015: The effect of increased convective entrainment on Asian monsoon biases in the MetUM general circulation model. *Quarterly Journal of the Royal Meteorological Society*, **141 (686)**, 311–326.

Carleton, A. M., D. A. Carpenter, and P. J. Weser, 1990: Mechanisms of interannual variability of the southwest United States summer rainfall maximum. *Journal of Climate*, **3 (9)**, 999–1015.

Chiriaco, M., S. Bastin, P. Yiou, M. Haeffelin, J.-C. Dupont, and M. Stéfanon, 2014: European heatwave in July 2006: Observations and modeling showing how local processes amplify conducive large-scale conditions. *Geophysical Research Letters*, **41 (15)**, 5644–5652.

Copernicus Climate Change Service (C3S), 2017: ERA5: Fifth generation of ECMWF atmospheric reanalyses of the global climate. *Copernicus Climate Change Service Climate Data Store (CDS)*, URL https://cds.climate.copernicus.eu/cdsapp#!/home.

Cui, J., L. Tian, Z. Wei, C. Huntingford, P. Wang, Z. Cai, N. Ma, and L. Wang, 2020: Quantifying the controls on evapotranspiration partitioning in the highest alpine meadow ecosystem. *Water Resources Research*, **56 (4)**, e2019WR024 815.

Curio, J., R. Schiemann, K. I. Hodges, and A. G. Turner, 2019: Climatology of Tibetan Plateau vortices in reanalysis data and a high-resolution global climate model. *Journal of Climate*, **32 (6)**, 1933–1950.

Diallo, I., Y. Xue, Q. Li, F. De Sales, and W. Li, 2019: Dynamical downscaling the impact of spring Western US land surface temperature on the 2015 flood extremes at the Southern Great Plains: effect of domain choice, dynamic cores and land surface parameterization. *Climate Dynamics*, **53 (1-2)**, 1039–1061.

Dorigo, W., and Coauthors, 2017: ESA CCI Soil Moisture for improved earth system understanding: State-of-the art and future directions. *Remote Sensing of Environment*, **203**, 185–215.

Duan, A., and G. Wu, 2005: Role of the Tibetan Plateau thermal forcing in the summer climate patterns over subtropical Asia. *Climate Dynamics*, **24 (7-8)**, 793–807.

Duan, A., and G. Wu, 2008: Weakening trend in the atmospheric heat source over the Tibetan Plateau during recent decades. Part I: Observations. *Journal of Climate*, **21 (13)**, 3149–3164.

Enomoto, T., B. J. Hoskins, and Y. Matsuda, 2003: The formation mechanism of the Bonin high in August. *Quarterly Journal of the Royal Meteorological Society: A journal of the atmospheric sciences, applied meteorology and physical oceanography*, **129 (587)**, 157–178.

Gallego-Elvira, B., C. M. Taylor, P. P. Harris, and D. Ghent, 2019: Evaluation of regional-scale soil moisture-surface flux dynamics in earth system models based on satellite observations of land surface temperature. *Geophysical Research Letters*, **46 (10)**, 5480–5488.

Gallego-Elvira, B., C. M. Taylor, P. P. Harris, D. Ghent, K. L. Veal, and S. S. Folwell, 2016: Global observational diagnosis of soil moisture control on the land surface energy balance. *Geophysical Research Letters*, **43 (6)**, 2623–2631.

Ge, J., Q. You, and Y. Zhang, 2019: Effect of Tibetan Plateau heating on summer extreme precipitation in eastern China. *Atmospheric Research*, **218**, 364–371.

Gruber, A., W. A. Dorigo, W. Crow, and W. Wagner, 2017: Triple collocation-based merging of satellite soil moisture retrievals. *IEEE Transactions on Geoscience and Remote Sensing*, **55 (12)**, 6780–6792.

Gruber, A., T. Scanlon, R. van der Schalie, W. Wagner, and W. Dorigo, 2019: Evolution of the ESA CCI Soil Moisture climate data records and their underlying merging methodology. *Earth System Science Data*, 1–37.

Gutzler, D. S., 2000: Covariability of spring snowpack and summer rainfall across the southwest United States. *Journal of Climate*, **13 (22)**, 4018–4027.

Hersbach, H., and Coauthors, 2018: Operational global reanalysis: progress, future directions and synergies with NWP. **(27)**, doi:10.21957/tkic6g3wm, URL https://www.ecmwf.int/node/18765.

Hersbach, H., and Coauthors, 2020: The ERA5 global reanalysis. *Quarterly Journal of the Royal Meteorological Society*, **146 (730)**, 1999–2049.

Hoinka, K. P., and M. D. Castro, 2003: The Iberian peninsula thermal low. *Quarterly Journal of the Royal Meteorological Society*, **129 (590)**, 1491–1511.

Howard, E., and R. Washington, 2018: Characterizing the synoptic expression of the Angola low. *Journal of Climate*, **31 (17)**, 7147–7165.

Hsu, H.-H., and S.-M. Lin, 2007: Asymmetry of the tripole rainfall pattern during the East Asian summer. *Journal of Climate*, **20 (17)**, 4443–4458.

Hu, Q., and S. Feng, 2004: A role of the soil enthalpy in land memory. *Journal of Climate*, **17 (18)**, 3633–3643.

Huffman, G. J., and Coauthors, 2007: The TRMM multisatellite precipitation analysis (TMPA): Quasi-global, multiyear, combined-sensor precipitation estimates at fine scales. *Journal of Hydrometeorology*, **8 (1)**, 38–55.

Jiang, D., Z. Ding, H. Drange, and Y. Gao, 2008: Sensitivity of East Asian climate to the progressive uplift and expansion of the Tibetan Plateau under the mid-Pliocene boundary conditions. *Advances in Atmospheric Sciences*, **25 (5)**, 709–722.

Kato, S., and Coauthors, 2018: Surface irradiances of edition 4.0 clouds and the earths radiant energy system (CERES) energy balanced and filled (EBAF) data product. *Journal of Climate*, **31 (11)**, 4501–4527.

Koster, R., S. Schubert, and M. Suarez, 2009: Analyzing the concurrence of meteorological droughts and warm periods, with implications for the determination of evaporative regime. *Journal of Climate*, **22 (12)**, 3331–3341.

683 Kutzbach, J., W. Prell, and W. F. Ruddiman, 1993: Sensitivity of Eurasian climate to surface uplift
684 of the Tibetan Plateau. *The Journal of Geology*, **101 (2)**, 177–190.

685 Lavender, S. L., C. M. Taylor, and A. J. Matthews, 2010: Coupled land–atmosphere intraseasonal
686 variability of the West African monsoon in a GCM. *Journal of climate*, **23 (21)**, 5557–5571.

687 Li, C., and M. Yanai, 1996: The onset and interannual variability of the Asian summer monsoon
688 in relation to land–sea thermal contrast. *Journal of Climate*, **9 (2)**, 358–375.

689 Liu, Y., G. Wu, J. Hong, B. Dong, A. Duan, Q. Bao, and L. Zhou, 2012: Revisiting Asian monsoon
690 formation and change associated with Tibetan Plateau forcing: II. Change. *Climate Dynamics*,
691 **39 (5)**, 1183–1195.

692 Lo, F., and M. P. Clark, 2002: Relationships between spring snow mass and summer precipitation
693 in the southwestern United States associated with the North American monsoon system. *Journal*
694 *of Climate*, **15 (11)**, 1378–1385.

695 Loeb, N. G., N. Manalo-Smith, S. Kato, W. F. Miller, S. K. Gupta, P. Minnis, and B. A. Wielicki,
696 2003: Angular distribution models for top-of-atmosphere radiative flux estimation from the
697 Clouds and the Earths Radiant Energy System instrument on the Tropical Rainfall Measuring
698 Mission satellite. Part I: Methodology. *Journal of Applied Meteorology*, **42 (2)**, 240–265.

699 Loikith, P. C., and A. J. Broccoli, 2012: Characteristics of observed atmospheric circulation pat-
700 terns associated with temperature extremes over North America. *Journal of Climate*, **25 (20)**,
701 7266–7281.

702 Lothon, M., F. Saïd, F. Lohou, and B. Campistron, 2008: Observation of the diurnal cycle in the
703 low troposphere of West Africa. *Monthly Weather Review*, **136 (9)**, 3477–3500.

Lu, R.-Y., J.-H. Oh, and B.-J. Kim, 2002: A teleconnection pattern in upper-level meridional wind over the North African and Eurasian continent in summer. *Tellus A: Dynamic Meteorology and Oceanography*, **54 (1)**, 44–55.

Mandke, S. K., A. Sahai, M. Shinde, S. Joseph, and R. Chattopadhyay, 2007: Simulated changes in active/break spells during the Indian summer monsoon due to enhanced CO2 concentrations: assessment from selected coupled atmosphere–ocean global climate models. *International Journal of Climatology: A Journal of the Royal Meteorological Society*, **27 (7)**, 837–859.

Minnis, P., and Coauthors, 2011: CERES edition-2 cloud property retrievals using TRMM VIRS and Terra and Aqua MODIS dataPart II: Examples of average results and comparisons with other data. *IEEE transactions on geoscience and remote sensing*, **49 (11)**, 4401–4430.

Miralles, D., M. Van Den Berg, A. Teuling, and R. De Jeu, 2012: Soil moisture-temperature coupling: A multiscale observational analysis. *Geophysical Research Letters*, **39 (21)**.

Molnar, P., P. England, and J. Martinod, 1993: Mantle dynamics, uplift of the Tibetan Plateau, and the Indian monsoon. *Reviews of Geophysics*, **31 (4)**, 357–396.

Notaro, M., and A. Zarrin, 2011: Sensitivity of the North American monsoon to antecedent Rocky Mountain snowpack. *Geophysical Research Letters*, **38 (17)**.

Parker, D., and Coauthors, 2005: The diurnal cycle of the West African monsoon circulation. *Quarterly Journal of the Royal Meteorological Society*, **131 (611)**, 2839–2860.

Quesada, B., R. Vautard, P. Yiou, M. Hirschi, and S. I. Seneviratne, 2012: Asymmetric European summer heat predictability from wet and dry southern winters and springs. *Nature Climate Change*, **2 (10)**, 736–741.

Rácz, Z., and R. K. Smith, 1999: The dynamics of heat lows. *Quarterly Journal of the Royal Meteorological Society*, **125 (553)**, 225–252.

Rajeevan, M., S. Gadgil, and J. Bhate, 2010: Active and break spells of the Indian summer monsoon. *Journal of Earth System Science*, **119 (3)**, 229–247.

Rienecker, M. M., and Coauthors, 2008: The GEOS-5 Data Assimilation System: Documentation of Versions 5.0. 1, 5.1. 0, and 5.2. 0.

Rodell, M., and Coauthors, 2004: The global land data assimilation system. *Bulletin of the American Meteorological Society*, **85 (3)**, 381–394.

Schumacher, D. L., J. Keune, C. C. Van Heerwaarden, J. V.-G. de Arellano, A. J. Teuling, and D. G. Miralles, 2019: Amplification of mega-heatwaves through heat torrents fuelled by upwind drought. *Nature Geoscience*, **12 (9)**, 712–717.

Schwingshackl, C., M. Hirschi, and S. I. Seneviratne, 2017: Quantifying spatiotemporal variations of soil moisture control on surface energy balance and near-surface air temperature. *Journal of Climate*, **30 (18)**, 7105–7124.

Shige, S., Y. Nakano, and M. K. Yamamoto, 2017: Role of orography, diurnal cycle, and intraseasonal oscillation in summer monsoon rainfall over the Western Ghats and Myanmar Coast. *Journal of Climate*, **30 (23)**, 9365–9381.

Singh, D., M. Tsiang, B. Rajaratnam, and N. S. Diffenbaugh, 2014: Observed changes in extreme wet and dry spells during the South Asian summer monsoon season. *Nature Climate Change*, **4 (6)**, 456.

Smith, R. K., and T. Spengler, 2011: The dynamics of heat lows over elevated terrain. *Quarterly Journal of the Royal Meteorological Society*, **137 (654)**, 250–263.

747 Spengler, T., M. J. Reeder, and R. K. Smith, 2005: The dynamics of heat lows in simple back-
748 ground flows. *Quarterly Journal of the Royal Meteorological Society*, **131 (612)**, 3147–3165.

749 Sperber, K., H. Annamalai, I.-S. Kang, A. Kitoh, A. Moise, A. Turner, B. Wang, and T. Zhou,
750 2013: The Asian summer monsoon: an intercomparison of CMIP5 vs. CMIP3 simulations of
751 the late 20th century. *Climate Dynamics*, **41 (9-10)**, 2711–2744.

752 Sultan, B., S. Janicot, and P. Drobinski, 2007: Characterization of the diurnal cycle of the West
753 African monsoon around the monsoon onset. *Journal of Climate*, **20 (15)**, 4014–4032.

754 Taylor, C. M., 2008: Intraseasonal land–atmosphere coupling in the west african monsoon. *Journal*
755 *of Climate*, **21 (24)**, 6636–6648.

756 Wan, B., Z. Gao, F. Chen, and C. Lu, 2017: Impact of Tibetan Plateau surface heating on persistent
757 extreme precipitation events in southeastern China. *Monthly Weather Review*, **145 (9)**, 3485–
758 3505.

759 Wang, B., Q. Bao, B. Hoskins, G. Wu, and Y. Liu, 2008: Tibetan Plateau warming and precipita-
760 tion changes in East Asia. *Geophysical Research Letters*, **35 (14)**.

761 Wang, M., and A. Duan, 2015: Quasi-biweekly oscillation over the Tibetan Plateau and its link
762 with the Asian summer monsoon. *Journal of Climate*, **28 (12)**, 4921–4940.

763 Wang, Z., A. Duan, and G. Wu, 2014: Time-lagged impact of spring sensible heat over the Tibetan
764 Plateau on the summer rainfall anomaly in East China: case studies using the WRF model.
765 *Climate Dynamics*, **42 (11-12)**, 2885–2898.

766 Weisheimer, A., F. J. Doblas-Reyes, T. Jung, and T. Palmer, 2011: On the predictability of the
767 extreme summer 2003 over Europe. *Geophysical Research Letters*, **38 (5)**.

Xue, Y., R. Vasic, Z. Janjic, Y. Liu, and P. C. Chu, 2012: The impact of spring subsurface soil temperature anomaly in the western US on North American summer precipitation: A case study using regional climate model downscaling. *Journal of Geophysical Research: Atmospheres*, **117 (D11)**.

Xue, Y., and Coauthors, 2016: Spring land temperature anomalies in northwestern US and the summer drought over Southern Plains and adjacent areas. *Environmental Research Letters*, **11 (4)**, 044 018.

Xue, Y., and Coauthors, 2018: Spring land surface and subsurface temperature anomalies and subsequent downstream late spring-summer droughts/floods in North America and East Asia. *Journal of Geophysical Research: Atmospheres*, **123 (10)**, 5001–5019.

Yao, T., J. Pu, A. Lu, Y. Wang, and W. Yu, 2007: Recent glacial retreat and its impact on hydrological processes on the Tibetan Plateau, China, and surrounding regions. *Arctic, Antarctic, and Alpine Research*, **39 (4)**, 642–650.

Yao, T., and Coauthors, 2012: Different glacier status with atmospheric circulations in Tibetan Plateau and surroundings. *Nature Climate Change*, **2 (9)**, 663–667.

Yasutomi, N., A. Hamada, and A. Yatagai, 2011: Development of a long-term daily gridded temperature dataset and its application to rain/snow discrimination of daily precipitation. *Global Environmental Research*, **15 (2)**, 165–172.

Yatagai, A., K. Kamiguchi, O. Arakawa, A. Hamada, N. Yasutomi, and A. Kitoh, 2012: APHRODITE: Constructing a long-term daily gridded precipitation dataset for Asia based on a dense network of rain gauges. *Bulletin of the American Meteorological Society*, **93 (9)**, 1401–1415.

790 Zampieri, M., F. DAndrea, R. Vautard, P. Ciais, N. de Noblet-Ducoudré, and P. Yiou, 2009: Hot
791 European summers and the role of soil moisture in the propagation of Mediterranean drought.
792 *Journal of Climate*, **22 (18)**, 4747–4758.

793 Zhisheng, A., J. E. Kutzbach, W. L. Prell, and S. C. Porter, 2001: Evolution of Asian monsoons and
794 phased uplift of the Himalaya–Tibetan plateau since Late Miocene times. *Nature*, **411 (6833)**,
795 62–66.

LIST OF FIGURES

Fig. 1. (a) Annual-mean power associated with 7 to 30 day variability of standardised JJA TRMM precipitation (filled, dimensionless). Cyan squares illustrate the location of weather stations in CMA whilst blue circles denote grid points in APHRODITE with measurements for a minimum of 95% boreal summer days between 1979 and 2015. TP is denoted by a black 3000 m contour. (b) Station-mean, annual-mean power in CMA (cyan) and APHRODITE (blue) JJA daily precipitation accumulations ([mm day^{-1}]^2). Vertical dashed grey lines denote 7 and 30 days. For both (a) and (b) only data between 2000 and 2015 is shown. (c) 5-day running-mean ESA CCI surface soil moisture observations (brown dots; m^3 m^{-3}) and CMA station-mean skin temperature anomalies (°C) at 00 (grey), 06 (purple), 12 (orange), and 18 (green) LST during JJA 2013. Cyan bars and blue dots denote CMA and APHRODITE station-mean daily precipitation accumulations (mm day^{-1}) respectively. . . . 41

Fig. 2. Mean surface characteristics across all local dry events in boreal summer recorded by the 49 CMA weather stations. (a) Six-hourly anomalous skin (cyan) and near-surface air temperatures (red, °C) along with composite-mean ESA CCI surface soil moisture observations (brown hexagons, m^3 m^{-3}). (b) 12 LST SEB components including surface upward longwave radiation ([Eqn. 1], orange), approximated surface SHF ([Eqn. 2], purple), CERES-derived sum of net-downward shortwave and longwave downward radiation (black), and LHF and G (red, W m^{-2}). Box-and-whisker plots denote daily precipitation accumulations (mm day^{-1}) during a dry event and the preceding six days. The orange line denotes the median; the top and bottom of the box denotes the upper and lower quartiles respectively; and the blue whiskers denote the 10th and 90th percentiles. Grey bars denote the number of events recorded for each dry event length. 42

Fig. 3. Anomalous station-mean surface characteristics preceding, during, and after a three-day regional dry event in the CMA dataset. A three-day regional dry event is defined when the station-mean precipitation accumulation is smaller than the twentieth percentile of JJA daily station-mean precipitation, denoted by the blue dashed horizontal line, for three days. (a) Anomalous station-mean near-surface air (red) and skin (cyan, °C) temperatures along with composite-mean ESA CCI surface soil moisture observations (brown hexagons, m^3 m^{-3}). (b) Surface upward longwave radiation ([Eqn. 1], orange), approximated surface SHF ([Eqn. 2], purple), CERES-derived sum of net-downward shortwave and longwave downward radiation (black), and LHF and G (red, W m^{-2}). Box-and-whisker plots show station-mean daily precipitation accumulations (mm day^{-1}). The orange line denotes the median; the top and bottom of the box denotes the upper and lower quartiles; and the blue whiskers denote the 10th and 90th percentiles. Filled blue circles denote outliers in precipitation rates. . . . 43

Fig. 4. Anomalous daily-mean near-surface air temperatures (°C, red line) during localised dry events in (a) CMA and (b) APHRODITE. Box-and-whisker plots denote daily precipitation accumulations (mm day^{-1}) during a dry event and the preceding six days. The orange line denotes the median; the top and bottom of the box denotes the upper and lower quartiles respectively; and the blue whiskers denote the 10th and 90th percentiles. Grey bars denote the number of events recorded for each dry event length. 44

Fig. 5. Composite-mean anomalies relative to the monthly-mean in geopotential height (m, filled contours) and horizontal wind (m s^{-1}, arrows) during days (a, d) 0.0, (b, e) 3.0, and (c, f) 6.0 of the three-day regional dry-spell composite at (a-c) 200 and (d-f) 500 hPa. For each pressure level, different colorbar limits and wind arrow sizes are used. The TP is denoted by a grey 3000m contour in each panel. Vertical blue lines at 75 and 105° longitude highlight TP's western and eastern boundaries. Orange horizontal lines at 30 and 40° latitude denotes the meridional range averaged for Hovmöllers (Fig. 6) and vertical composites (Fig. 8).

Only data significant at the 95% confidence level is shown with wind vectors displayed if significant in either a zonal or meridional direction. 45

Fig. 6. Hovmöllers of ERA5 composite-mean, meridional-mean (30 to 40° latitude) anomalies in (a) vertically-averaged meridional wind (m s^{-1}) between 200 and 450 hPa, (b, c) geopotential height (m) at (b) 200 and (c) 500 hPa, and (d, e) temperature (°C) at (d) 200 and (e) 500 hPa in the three-day regional dry-event composite. Vertical black dashed lines at 75 and 105° longitude highlight TP's western and eastern boundaries whilst horizontal dashed lines denote days 0.0 and 3.0 of the regional dry event composite. Stippling denotes anomalies significant at the 95% confidence level. 46

Fig. 7. Composite-mean, regional-mean (30 to 40° latitude, 90 to 100° longitude) anomalous (a) temperature (°C), (b) geopotential height (m), (c) surface pressure (hPa), and (d) relative vorticity (s^{-1}) during the three-day regional dry event composite. For a, b, and d, anomalous values are shown at 500 (red), 400 (orange), 300 (cyan), and 200 (blue) hPa. Box-and-whisker plots in all panels show station-mean daily precipitation accumulations (mm day^{-1}). Upper and lower quartiles are denoted by the top and bottom of boxes; box whiskers denote the 10th and 90th percentiles; and the mean is denoted by an orange line. Background colours in each panel highlight daytime (yellow, 06 to 18 LST) and nighttime (purple, 18 to 06 LST) hours. 47

Fig. 8. Changes in composite-mean, daily-mean, meridional-mean (30 to 40° latitude) (a, c, e, g) temperature (filled, °C), zonal wind (lined, m s^{-1}), (b, d, f, i) geopotential height (filled, m), and vertical wind (lined, hPa s^{-1}) between (a, b) 00 to 06, (c, d) 06 to 12, (e, f) 12 to 18, and (g, h) 18 to 00 LST during the three days of minimal regional precipitation in the three-day regional dry-event composite. Zonal and vertical wind changes are in intervals of 0.3 m s^{-1} and 1.5 $\times$ 10^{-4} hPa s^{-1} respectively with solid/dashed lines denoting positive/negative values. The dotted contour denotes the zeroth value. Grey shading in each panel denotes the minimum surface pressure observed at each longitude in the regional three-day dry event composite. 48

Fig. 9. Composite-mean, daily-mean changes in relative vorticity (filled, s^{-1}) and horizontal wind (arrows, m s^{-1}) at 500 hPa between (a) 00 to 06, (b) 06 to 12, (c) 12 to 18, and (d) 18 to 00 LST during three days of minimal TP precipitation in the dry event composite. Horizontal wind is regridded to 2° latitude and longitude for relative vorticity tendencies. The TP is denoted by a 3000m grey contour in each panel. A horizontal wind scale is shown to the bottom right of each panel. 49

Fig. 10. (a, b) Mean state (a) temperature (filled, °C) at 200 hPa and (b) geopotential height (filled, m) at 850 hPa during day 3.0 of the regional dry event composite. Arrows denote mean state horizontal winds at (a) 200 and (b) 850 hPa. (c-f) Composite-mean anomalies relative to the monthly-mean in (c, e) temperature (°C, filled contours) at 200 hPa and (d, f) geopotential height (m, filled) at 850 hPa during days (c, d) 3.0, and (e, f) 6.0 of the regional dry event composite. The TP is denoted by a grey 3000m contour in each panel. Vertical dashed black lines at 75 and 105° longitude highlight TP's western and eastern boundaries. Orange horizontal lines at 30 and 40° latitude denotes the meridional range averaged for Hovmöllers (Fig. 6) and vertical composites (Fig. 8). Grey stippling denotes significance at the 95% confidence level. Regions filled in white in panels b, d, and f denotes locations where the surface is above 850 hPa. 50

Fig. 11. Changes in average (a, c, e, g) daily-accumulated precipitation (mm day^{-1}) and (b, d, f, h) daily-mean temperature (°C) in days (a, b) 3.0, (c, d) 4.0, (e, f) 5.0, and (g, h) 6.0 of the regional three-day dry event composite compared to the boreal summer average. Stippling

denotes a significant change in mean precipitation and temperature at a 95% confidence level. TP is denoted by a 3000m contour in each panel. 51

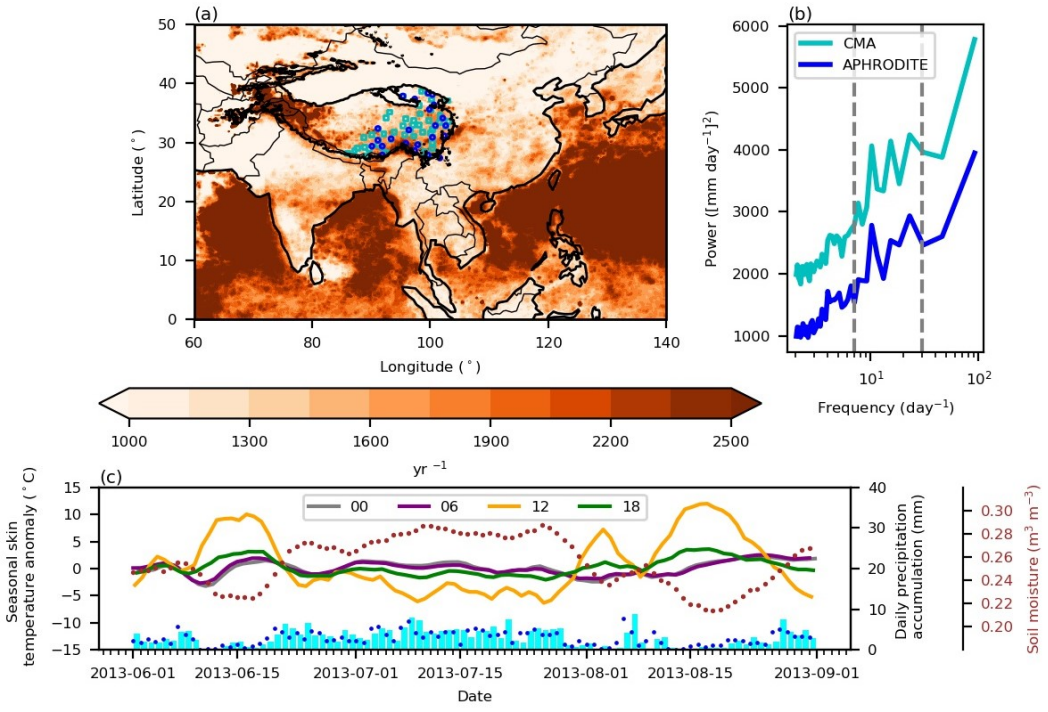

FIG. 1. (a) Annual-mean power associated with 7 to 30 day variability of standardised JJA TRMM precipitation (filled, dimensionless). Cyan squares illustrate the location of weather stations in CMA whilst blue circles denote grid points in APHRODITE with measurements for a minimum of 95% boreal summer days between 1979 and 2015. TP is denoted by a black 3000 m contour. (b) Station-mean, annual-mean power in CMA (cyan) and APHRODITE (blue) JJA daily precipitation accumulations ([mm day^{-1}]^2). Vertical dashed grey lines denote 7 and 30 days. For both (a) and (b) only data between 2000 and 2015 is shown. (c) 5-day running-mean ESA CCI surface soil moisture observations (brown dots; m^3 m^{-3}) and CMA station-mean skin temperature anomalies (°C) at 00 (grey), 06 (purple), 12 (orange), and 18 (green) LST during JJA 2013. Cyan bars and blue dots denote CMA and APHRODITE station-mean daily precipitation accumulations (mm day^{-1}) respectively.

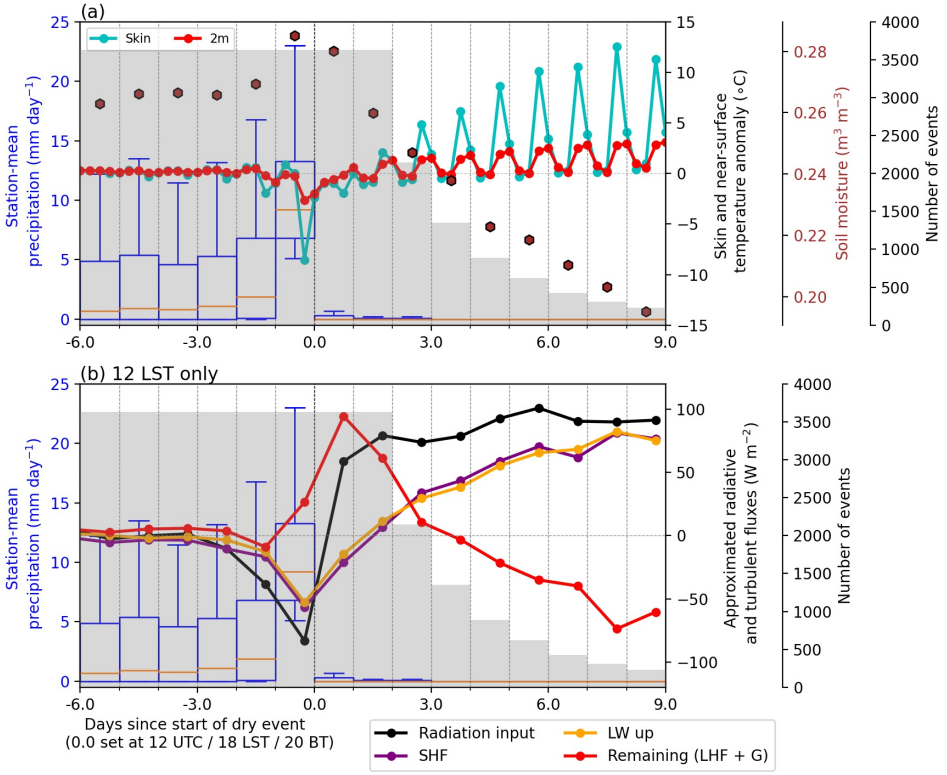

902 FIG. 2. Mean surface characteristics across all local dry events in boreal summer recorded by the 49 CMA
903 weather stations. (a) Six-hourly anomalous skin (cyan) and near-surface air temperatures (red, °C) along with
904 composite-mean ESA CCI surface soil moisture observations (brown hexagons, m^3 m^{-3}). (b) 12 LST SEB
905 components including surface upward longwave radiation ([Eqn. 1], orange), approximated surface SHF ([Eqn.
906 2], purple), CERES-derived sum of net-downward shortwave and longwave downward radiation (black), and
907 LHF and G (red, W m^{-2}). Box-and-whisker plots denote daily precipitation accumulations (mm day^{-1}) during
908 a dry event and the preceding six days. The orange line denotes the median; the top and bottom of the box
909 denotes the upper and lower quartiles respectively; and the blue whiskers denote the 10th and 90th percentiles.
910 Grey bars denote the number of events recorded for each dry event length.

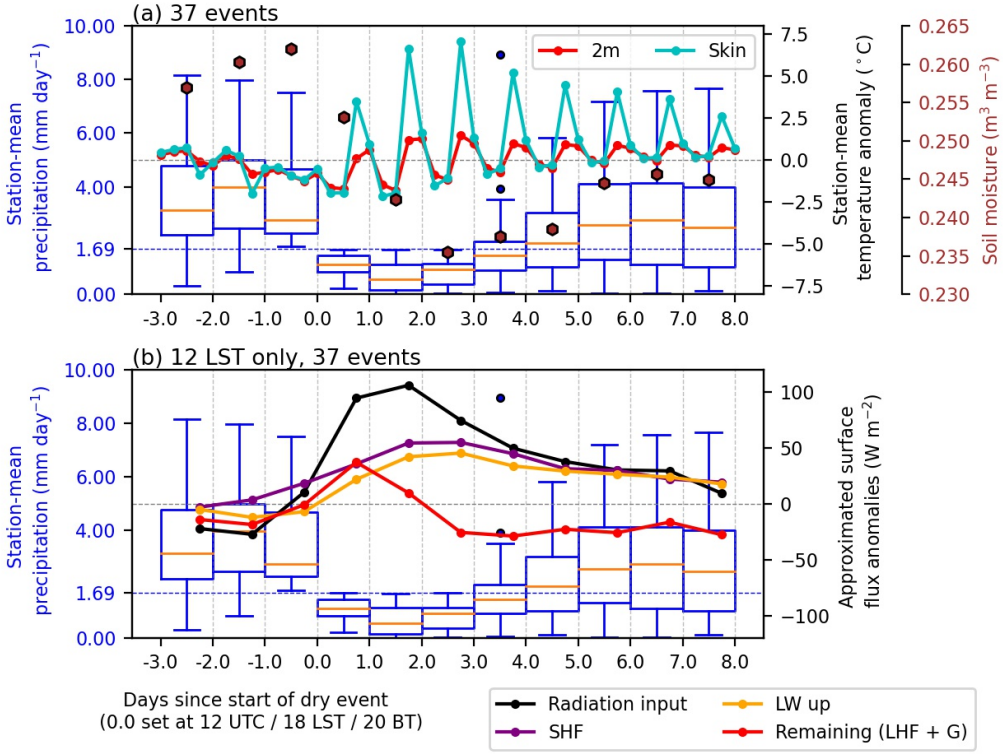

911 FIG. 3. Anomalous station-mean surface characteristics preceding, during, and after a three-day regional
912 dry event in the CMA dataset. A three-day regional dry event is defined when the station-mean precipitation
913 accumulation is smaller than the twentieth percentile of JJA daily station-mean precipitation, denoted by the
914 blue dashed horizontal line, for three days. (a) Anomalous station-mean near-surface air (red) and skin (cyan,
915 °C) temperatures along with composite-mean ESA CCI surface soil moisture observations (brown hexagons, m^3
916 m^{-3}). (b) Surface upward longwave radiation ([Eqn. 1], orange), approximated surface SHF ([Eqn. 2], purple),
917 CERES-derived sum of net-downward shortwave and longwave downward radiation (black), and LHF and G
918 (red, W m^{-2}). Box-and-whisker plots show station-mean daily precipitation accumulations (mm day^{-1}). The
919 orange line denotes the median; the top and bottom of the box denotes the upper and lower quartiles; and the
920 blue whiskers denote the 10th and 90th percentiles. Filled blue circles denote outliers in precipitation rates.

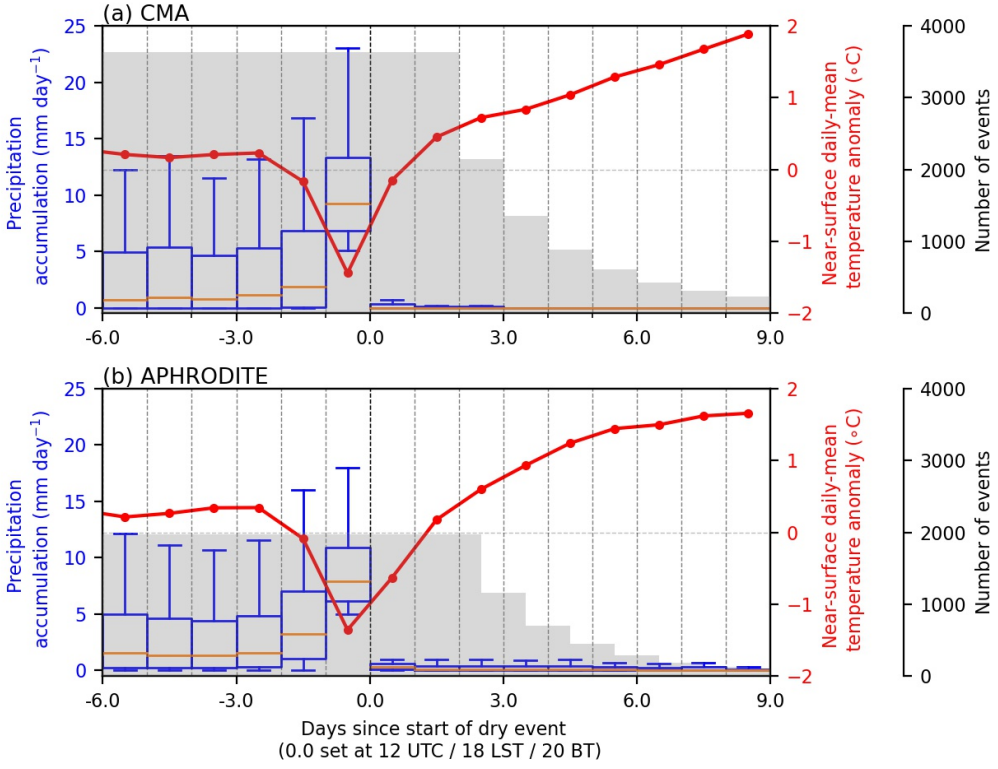

FIG. 4. Anomalous daily-mean near-surface air temperatures (°C, red line) during localised dry events in (a) CMA and (b) APHRODITE. Box-and-whisker plots denote daily precipitation accumulations (mm day^{-1}) during a dry event and the preceding six days. The orange line denotes the median; the top and bottom of the box denotes the upper and lower quartiles respectively; and the blue whiskers denote the 10th and 90th percentiles. Grey bars denote the number of events recorded for each dry event length.

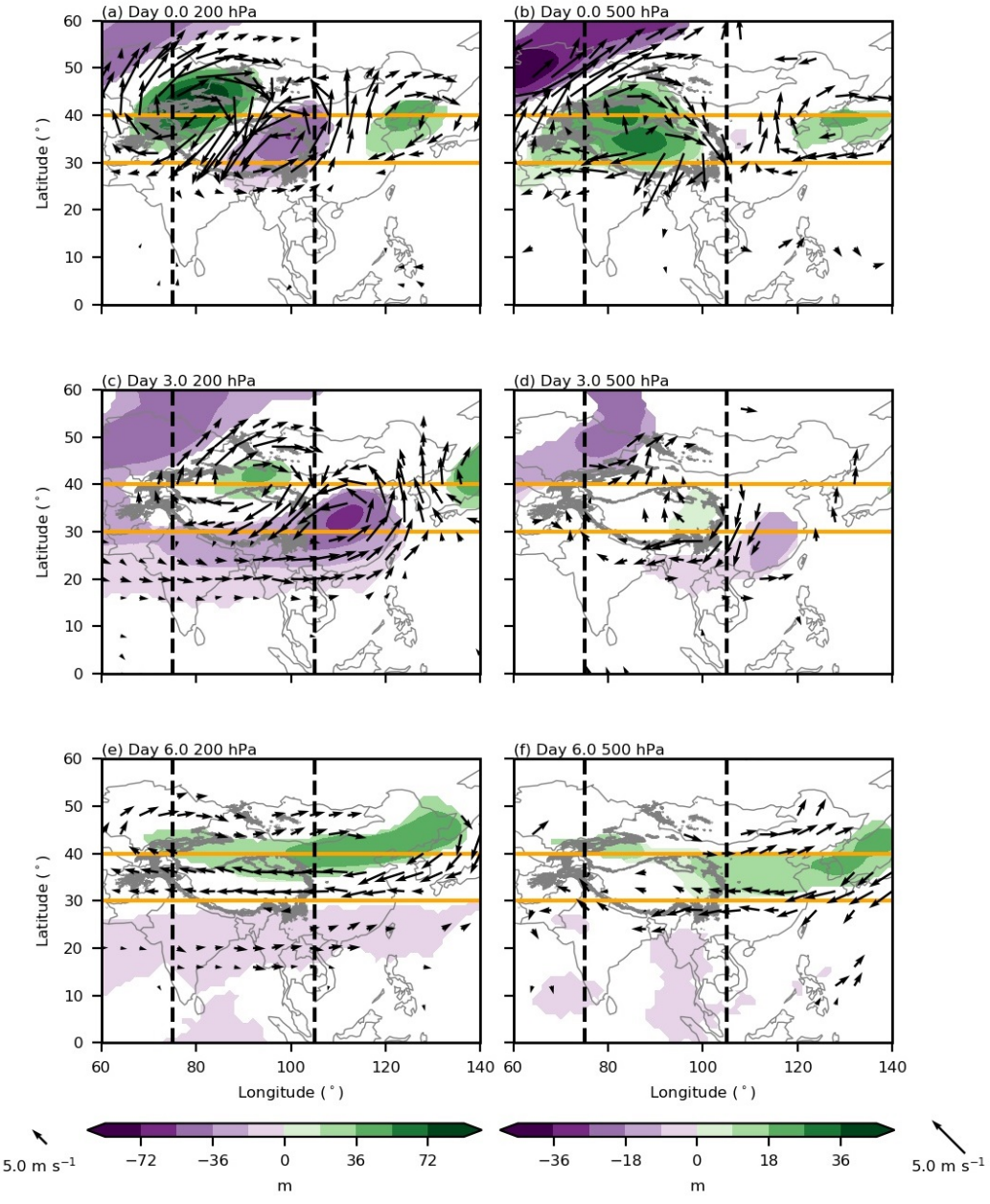

926 FIG. 5. Composite-mean anomalies relative to the monthly-mean in geopotential height (m, filled contours)
927 and horizontal wind (m s^{-1}, arrows) during days (a, d) 0.0, (b, e) 3.0, and (c, f) 6.0 of the three-day regional
928 dry-spell composite at (a-c) 200 and (d-f) 500 hPa. For each pressure level, different colorbar limits and wind
929 arrow sizes are used. The TP is denoted by a grey 3000m contour in each panel. Vertical blue lines at 75 and
930 105° longitude highlight TP's western and eastern boundaries. Orange horizontal lines at 30 and 40° latitude
931 denotes the meridional range averaged for Hovmöllers (Fig. 6) and vertical composites (Fig. 8). Only data
932 significant at the 95% confidence level is shown with wind vectors displayed if significant in either a zonal or
933 meridional direction.

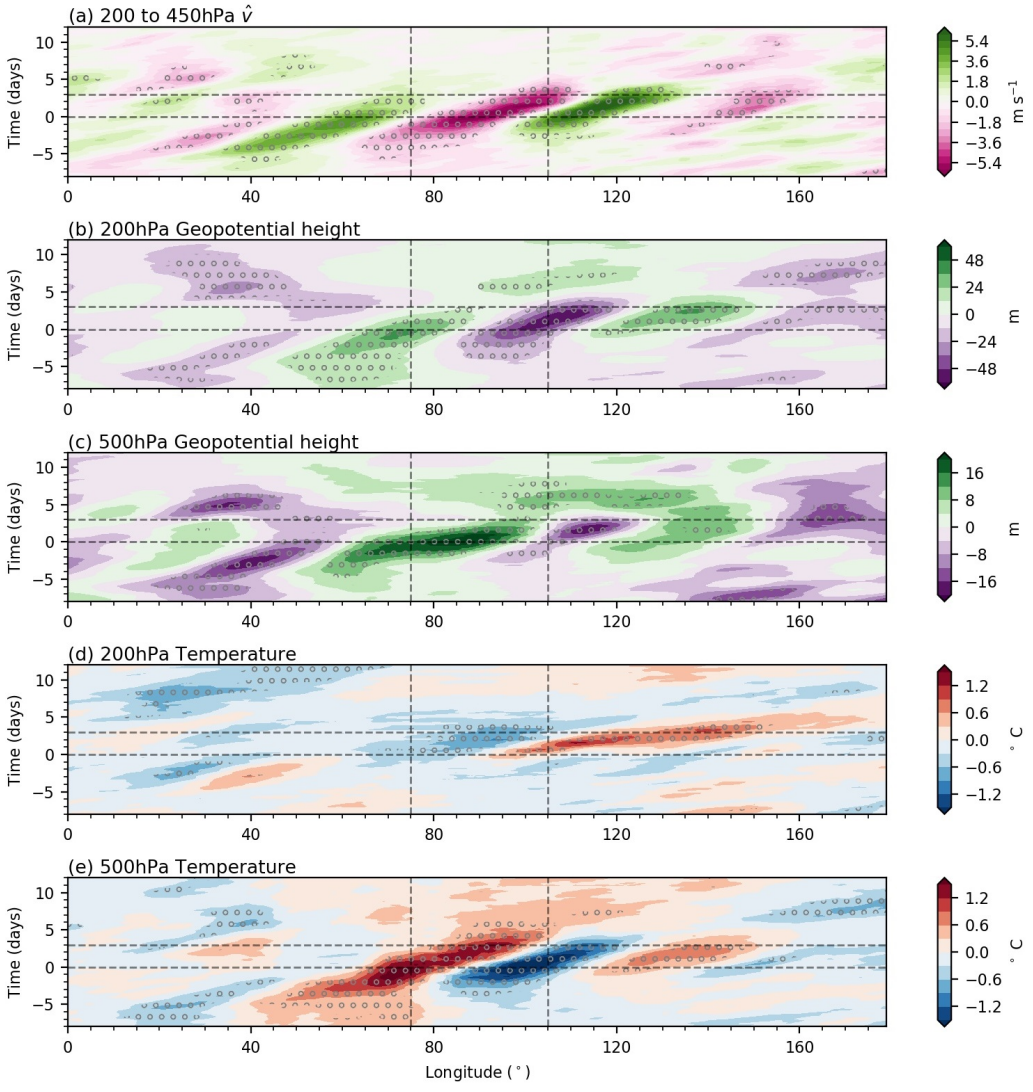

934 FIG. 6. Hovmöllers of ERA5 composite-mean, meridional-mean (30 to 40° latitude) anomalies in (a)
935 vertically-averaged meridional wind (m s^{-1}) between 200 and 450 hPa, (b, c) geopotential height (m) at (b)
936 200 and (c) 500 hPa, and (d, e) temperature (°C) at (d) 200 and (e) 500 hPa in the three-day regional dry-event
937 composite. Vertical black dashed lines at 75 and 105° longitude highlight TP's western and eastern boundaries
938 whilst horizontal dashed lines denote days 0.0 and 3.0 of the regional dry event composite. Stippling denotes
939 anomalies significant at the 95% confidence level.

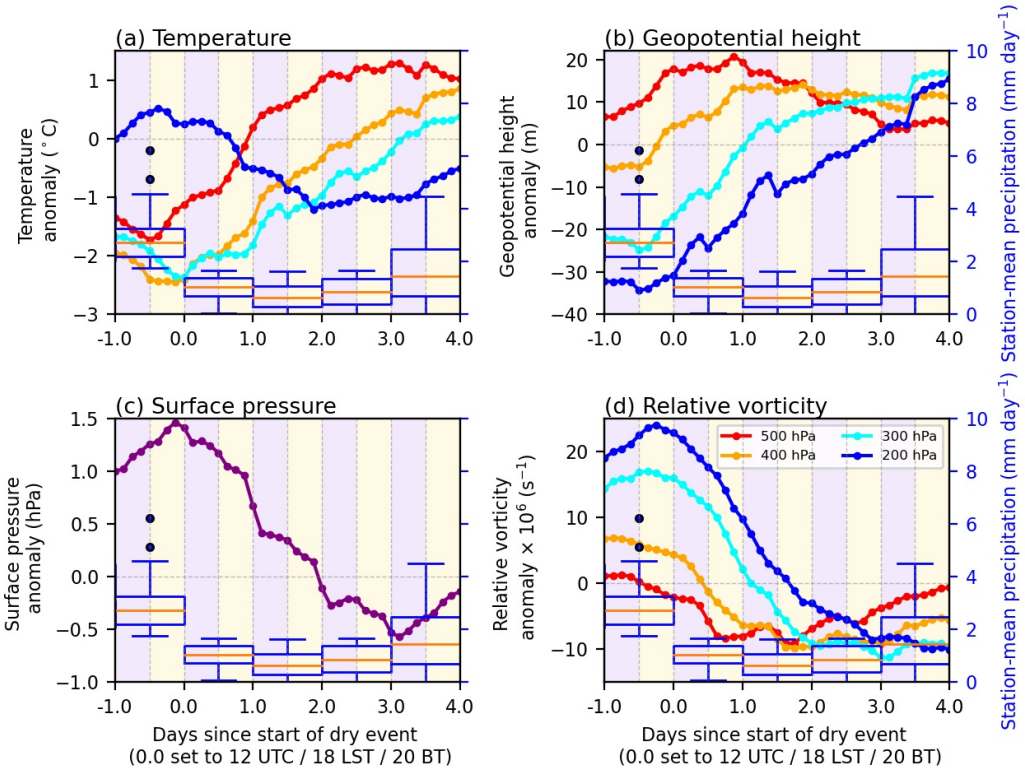

940 FIG. 7. Composite-mean, regional-mean (30 to 40° latitude, 90 to 100° longitude) anomalous (a) temperature
941 (°C), (b) geopotential height (m), (c) surface pressure (hPa), and (d) relative vorticity (s^{-1}) during the three-day
942 regional dry event composite. For a, b, and d, anomalous values are shown at 500 (red), 400 (orange), 300 (cyan),
943 and 200 (blue) hPa. Box-and-whisker plots in all panels show station-mean daily precipitation accumulations
944 (mm day^{-1}). Upper and lower quartiles are denoted by the top and bottom of boxes; box whiskers denote
945 the 10th and 90th percentiles; and the mean is denoted by an orange line. Background colours in each panel
946 highlight daytime (yellow, 06 to 18 LST) and nighttime (purple, 18 to 06 LST) hours.

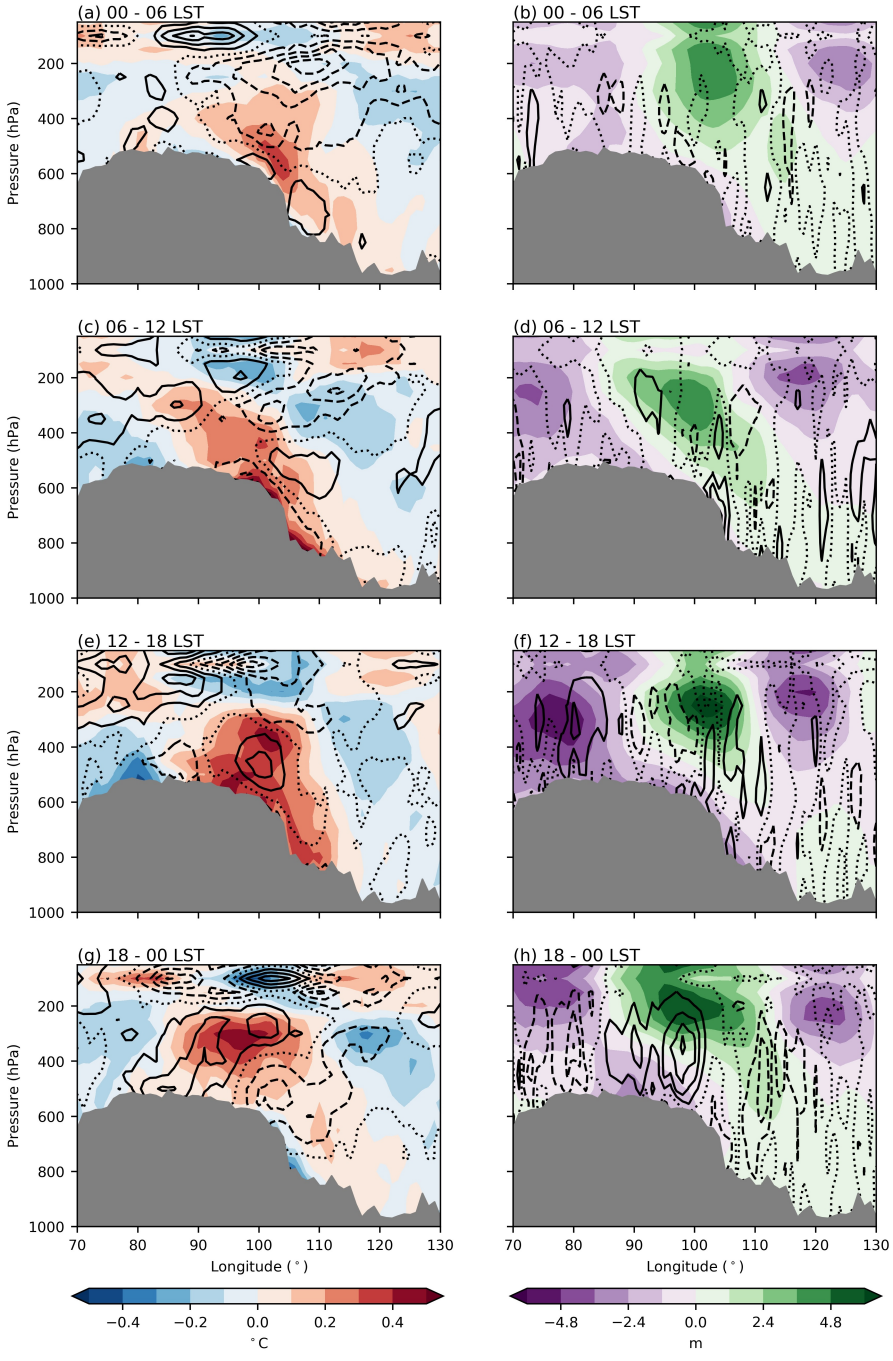

947 FIG. 8. Changes in composite-mean, daily-mean, meridional-mean (30 to 40° latitude) (a, c, e, g) temperature
948 (filled, °C), zonal wind (lined, m s^{-1}), (b, d, f, i) geopotential height (filled, m), and vertical wind (lined, hPa s^{-1})
949 between (a, b) 00 to 06, (c, d) 06 to 12, (e, f) 12 to 18, and (g, h) 18 to 00 LST during the three days of minimal
950 regional precipitation in the three-day regional dry-event composite. Zonal and vertical wind changes are in
951 intervals of 0.3 m s^{-1} and 1.5 $\times$ 10^{-4} hPa s^{-1} respectively with solid/dashed lines denoting positive/negative
952 values. The dotted contour denotes the zeroth value. Grey shading in each panel denotes the minimum surface
953 pressure observed at each longitude in the regional three-day dry event composite.

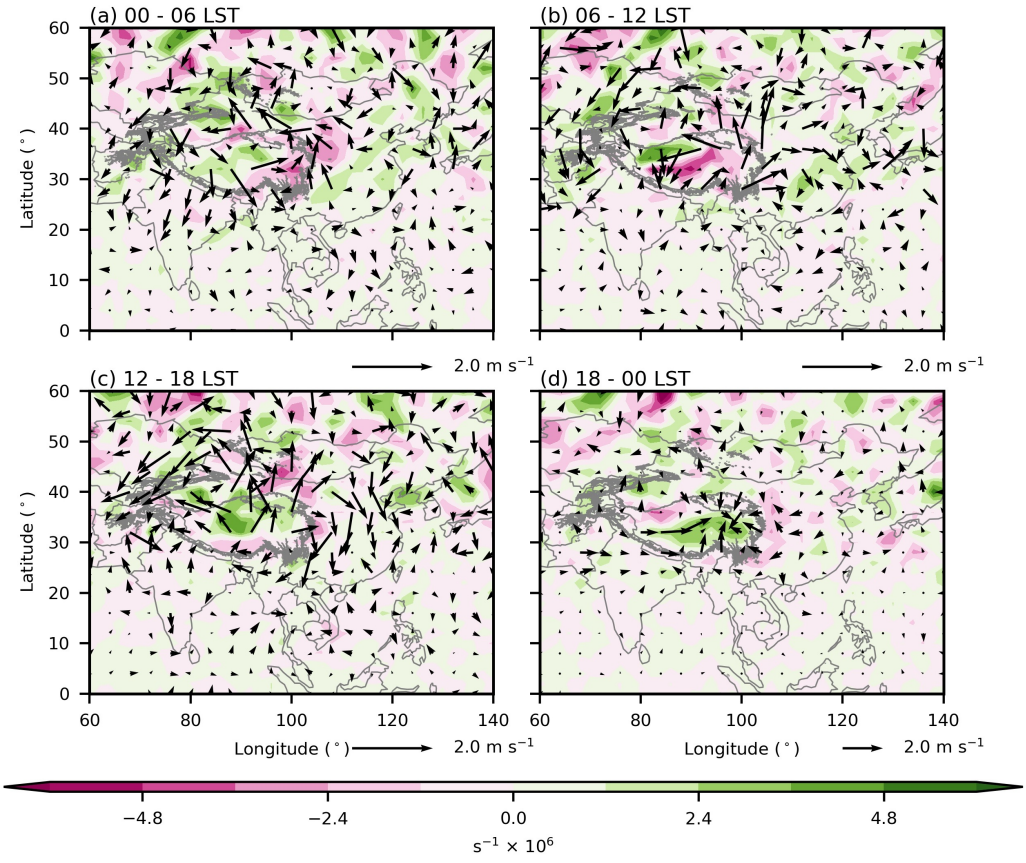

954 FIG. 9. Composite-mean, daily-mean changes in relative vorticity (filled, s^{-1}) and horizontal wind (arrows,
955 m s^{-1}) at 500 hPa between (a) 00 to 06, (b) 06 to 12, (c) 12 to 18, and (d) 18 to 00 LST during three days of
956 minimal TP precipitation in the dry event composite. Horizontal wind is regridded to 2° latitude and longitude
957 for relative vorticity tendencies. The TP is denoted by a 3000m grey contour in each panel. A horizontal wind
958 scale is shown to the bottom right of each panel.

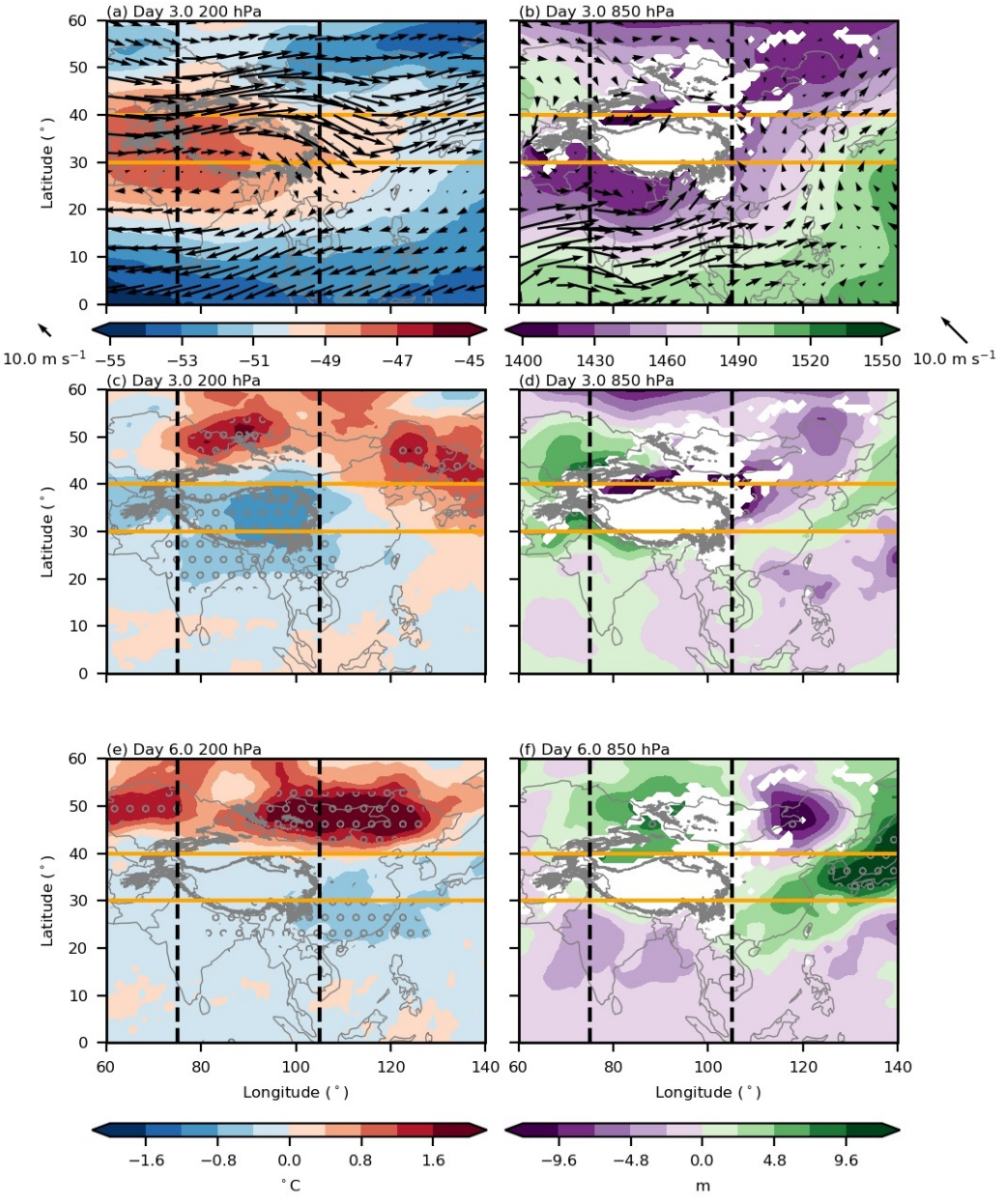

FIG. 10. (a, b) Mean state (a) temperature (filled, °C) at 200 hPa and (b) geopotential height (filled, m) at 850 hPa during day 3.0 of the regional dry event composite. Arrows denote mean state horizontal winds at (a) 200 and (b) 850 hPa. (c-f) Composite-mean anomalies relative to the monthly-mean in (c, e) temperature (°C, filled contours) at 200 hPa and (d, f) geopotential height (m, filled) at 850 hPa during days (c, d) 3.0, and (e, f) 6.0 of the regional dry event composite. The TP is denoted by a grey 3000m contour in each panel. Vertical dashed black lines at 75 and 105° longitude highlight TP's western and eastern boundaries. Orange horizontal lines at 30 and 40° latitude denotes the meridional range averaged for Hovmöllers (Fig. 6) and vertical composites (Fig. 8). Grey stippling denotes significance at the 95% confidence level. Regions filled in white in panels b, d, and f denotes locations where the surface is above 850 hPa.

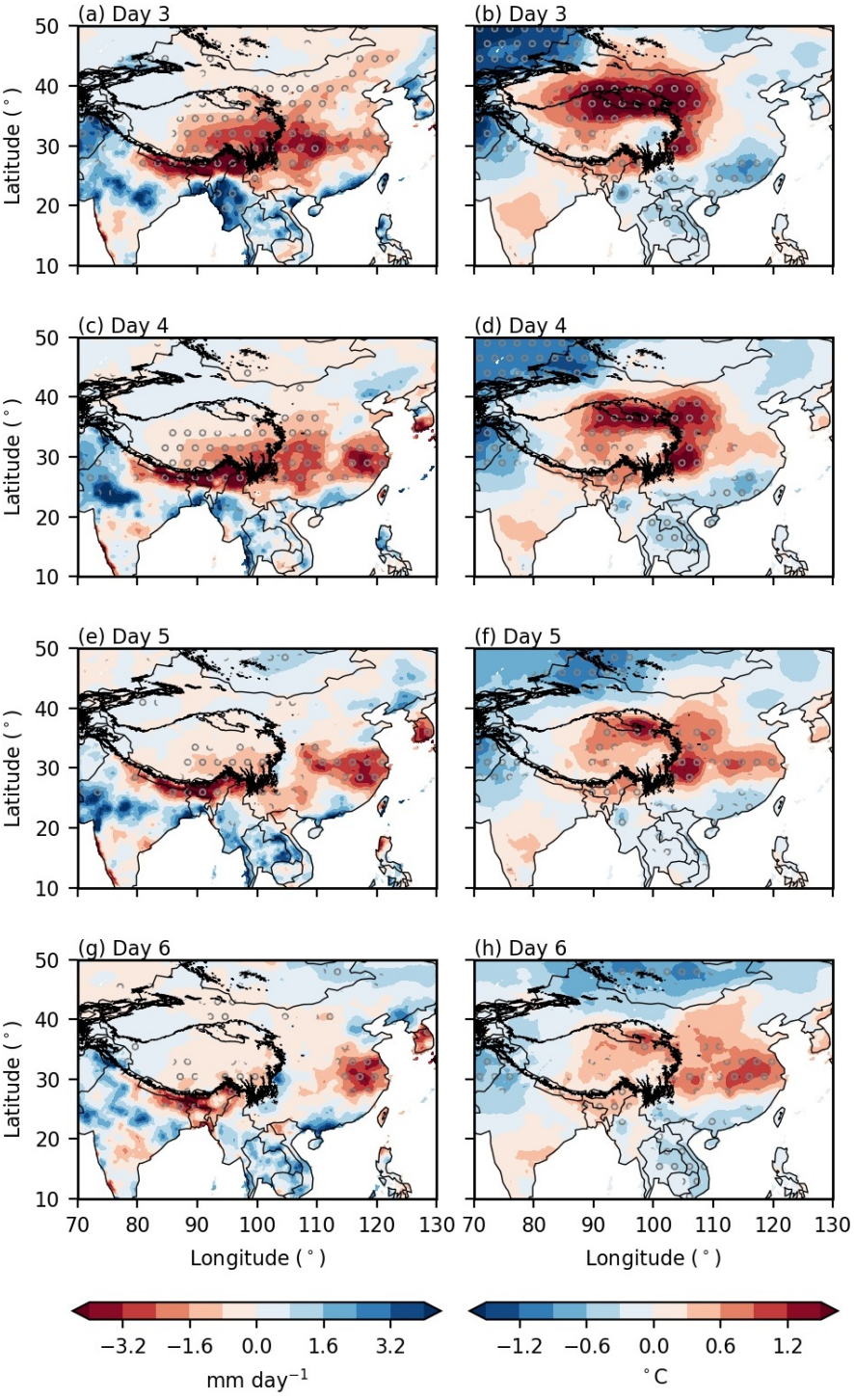

FIG. 11. Changes in average (a, c, e, g) daily-accumulated precipitation (mm day^{-1}) and (b, d, f, h) daily-mean temperature (°C) in days (a, b) 3.0, (c, d) 4.0, (e, f) 5.0, and (g, h) 6.0 of the regional three-day dry event composite compared to the boreal summer average. Stippling denotes a significant change in mean precipitation and temperature at a 95% confidence level. TP is denoted by a 3000m contour in each panel.